Impact of geodynamics on fluid circulation and diagenesis of carbonate reservoirs in a foreland basin: Example of the Upper Lacq reservoir (Aquitaine basin, SW France)

Alexy Elias Bahnan, Cédric Carpentier, Jacques Pironon, Mary Ford, Maxime Ducoux, Guillaume Barre, Xavier Mangenot, Eric C. Gaucher

Impact of geodynamics on fluid circulation and diagenesis of carbonate reservoirs in a foreland basin: example of the Upper Lacq reservoir (Aquitaine basin, SW France)

Alexy ELIAS BAHNAN[1,2*], Cédric CARPENTIER[1], Jacques PIRONON[1] , Mary FORD[1,3], Maxime DUCOUX[2,4], Guillaume BARRÉ[2,], Xavier MANGENOT[2,5] and Eric C. GAUCHER[2]

[1]Université de Lorraine, CNRS, CREGU, GeoRessources lab, BP 70239, F-54506 Vandœuvre-lès-Nancy, France

[2]TOTAL, CSTJF, F-64018 Pau Cedex, France

[3]CRPG, UMR 7358, 15 Rue Notre Dame des Pauvres, 54501 Vandœuvre-lès-Nancy, France

[4]CNRS/TOTAL/Univ. Pau & Pays Adour/ E2S UPPA, Laboratoire des Fluides Complexes et leurs Réservoirs-IPRA, UMR5150, 64000, PAU, France

[5]California Institute of Technology, Division of Geological and Planetary Sciences, 1200 E California Blvd | Pasadena, CA 91125, USA

*E-mail address: alexy.elias-bahnan@univ-lorraine.fr

20 Abstract

21 Orogeny-driven fluids that circulate in foreland basins can have strong impacts on
22 petroleum systems and reservoir properties. This applies to the Upper Cretaceous Lacq
23 reservoir of the Aquitaine Basin in southwestern France located north of the Pyrenean
24 Mountains. We study a drillcore from a 650 m deep oil reservoir to document how the
25 evolution of a foreland basin, which formed after a hyperextension phase, affected fluid
26 circulation and eventually reservoir diagenesis. Using drillcore samples, petrographic
27 observations, fluid inclusion studies coupled with thermodynamic modeling, isotopic and
28 rare earth element geochemistry, as well as basin modeling were performed to investigate
29 and describe the fluid types and sources, the pressure-temperature evolution and the
30 timing of diagenetic fluid flow. Early diagenesis involves some bacterial activity
31 represented by micrite rims and framboidal pyrites, as well as early dolomitization involving
32 a mixture of meteoric and formation fluids. During burial, dolomite overgrowth, saddle
33 dolomites, coarse blocky calcites and anhydrites precipitate. The last products consist of
34 iron oxide precipitation and meteoric recharge of the reservoir with groundwater. Our
35 results indicate that after the deposition of the Paleocene flysch formation, Mg-rich, low
36 salinity, hot, and relatively deep clay-released fluids migrated along thrust faults from
37 deeper parts of the basin during the climax of the compressional Pyrenean phase
38 (Eocene). They acted as dolomitizing hydrothermal fluids with a thermal disequilibrium in
39 the order of 30-40°C hotter than the ambient host rocks. Another orogeny-driven,
40 hydrothermal and Mg-poor fluid mixed with oil generated by Jurassic-Barremian source
41 rocks and precipitated calcites and anhydrites. Finally, during uplift, oxidizing fluids were
42 laterally introduced as the present-day groundwater. Hence, by combining different
43 petrographic, geochemical and modeling proxies, we document how the Eocene orogenic
44 phase played a crucial role in basin-scale fluid flow and carbonate diagenesis.

45 *Keywords:* carbonate diagenesis, Pyrenees, Aquitaine foreland basin, Upper Lacq
46 reservoirs, fluid inclusions, basin modeling, dolomitization, hydrothermal fluids.

1 Introduction

The geodynamic evolution of basins exerts a major control on the evolution of the pathways, temperature, pressure and chemistry of circulating fluids (Vilasi et al., 2006; López-Horgue et al., 2010; Beaudoin et al., 2011; Evans and Fischer, 2012; Vandeginste et al., 2013; Mangenot et al., 2018a). This in turn influences the diagenesis and petrophysical properties of petroleum reservoirs. Many dolomitized carbonate reservoirs worldwide have been interpreted as formed during early diagenesis in shallow peritidal environments (Koehrer et al., 2010; Moore, 2013; Swart et al., 2005; Walls and Burrowes, 1985). However, several studies demonstrate that processes of pervasive dolomitization can be linked to the impact of deep hot hydrothermal fluids percolating along structural pathways (Machel and Anderson, 1989; Boni et al., 2000; Swennen et al., 2003; Davies and Smith, 2006; Gasparrini et al., 2006; López-Horgue et al., 2010; Gomez-Rivas et al., 2014; Salardon et al., 2017). In the Aquitaine basin (SW France), several hydrocarbon fields are located in Jurassic and Cretaceous dolomites, where dolomitization is interpreted to be the result of early diagenesis (Biteau et al., 2006). First studies of the Lacq reservoirs, considered as the largest and most strategic hydrocarbon-producing reservoirs in France (Biteau et al., 2006), date back to the 1950s with the initial drilling of the Lacq-1 well. Several models were proposed to explain the diagenesis and petrophysical properties of the reservoir. Initially, dolomitization of the shallow marine carbonates of the Upper Lacq reservoir was considered to be due to early diagenesis, and to impact preferentially the more bioclastic facies (Bouroullec et al., 1986). Therefore, in this initial model fluid circulation, diagenesis, and reservoir properties were mainly controlled by the distribution of primary sedimentary fabrics. However, even if an early diagenetic origin for dolomitization was proposed, no clear petrographic or geochemical evidence were provided by authors and little was known about the nature, timing, and origin of dolomitization fluids that flowed in these reservoirs. Recently, geodynamic models of the Pyrenees and the south Aquitaine basin have been revisited and updated to include

74 the involvement of a late early Cretaceous rifting phase that evolved to extreme crustal
75 thinning coupled with mantle exhumation (Lagabrielle and Bodinier, 2008; Jammes et al.,
76 2009, 2010a,b; Roca et al., 2011;. Clerc and Lagabrielle, 2014; Masini et al., 2014;
77 Mouthereau et al., 2014; Tugend et al., 2015; Corre et al., 2016; Teixell et al., 2016;
78 Vacherat et al., 2016). This event was followed by an inversion and the main Pyrenean
79 convergence during the late Cretaceous and the Paleogene. This revised model highlights
80 the possible impact of hydrothermal fluids on the diagenesis of petroleum reservoirs in the
81 southern Aquitaine Basin (Jammes et al., 2009, 2010; Lagabrielle et al., 2010; Clerc and
82 Lagabrielle, 2014; Clerc et al., 2015; Salardon et al., 2016; Renard et al., 2019). In this
83 context a reexamination of the diagenetic evolution of these reservoirs must be performed.
84 Given its complex geodynamic history and the abundance of subsurface data, the
85 Aquitaine Basin serves as a natural laboratory to study how the structural evolution of the
86 Pyrenean foreland domain influenced fluid circulation and eventually reservoir diagenesis
87 (Moore, 2013; Corre et al., 2018; Haile et al., 2018).

88 This study focuses on the Upper Cretaceous reservoirs (from Coniacian to Campanian in
89 age) and aims to reappraise the diagenetic model by combining results from recent
90 analytical methods (e.g. fluid inclusion modeling, clumped isotope thermometry…) and to
91 identify the different fluid types involved at different phases of the geologic history. The
92 final objective is to correlate the timing of fluid circulations with the geodynamic evolution
93 of the basin.

94 ## 2 Geological setting and stratigraphic framework

95 The Lacq petroleum system is one of the largest petroleum fields in the Arzacq sub-basin,
96 of the Aquitaine basin (Fig. 1). It consists of a salt-cored anticline whose axis is oriented
97 NW-SE (Fig. 2). This anticline is an elevated structure relative to the surrounding Lower
98 Cretaceous sub-basins (Southern Lacq, North Arzacq and East Arzacq basins (Fig.1) that
99 were formed during the major rifting phase that created the V-shaped Bay of Biscay to the
100 west (Biteau et al., 2006). These rift basins formed part of the European rifted margin. The

proximal Arzacq rift was separated from the hyper-extended Mauléon rift basin to the south by the Grand Rieu Ridge, a tilted basement block (Figs 1 and 2) (Masini et al., 2014).

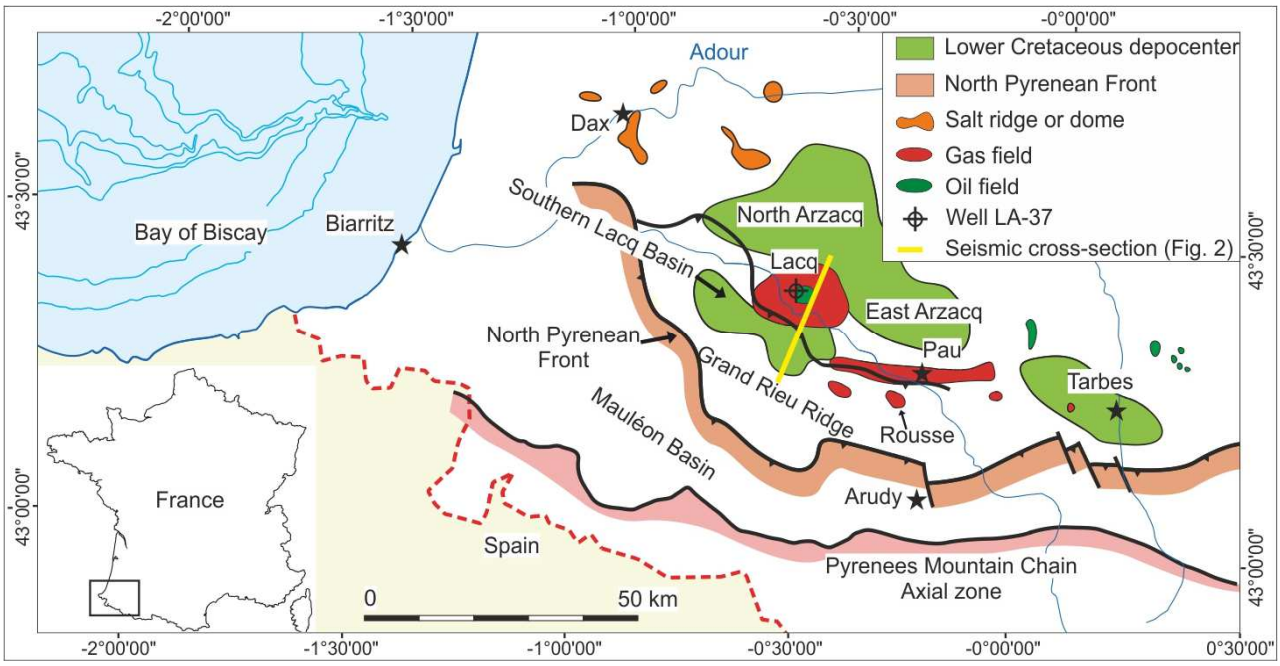

Figure 1. Structural sketch map of the SW Aquitaine basin, showing the principal structural elements, Cretaceous rift basins and hydrocarbon fields (modified after Biteau et al., 2006).

The petroleum system encompasses two economically important reservoirs. The first is the Upper Lacq reservoir located at 650m depth and sealed by the overlying Paleocene Flysch (Fig. 2). The reservoir produced heavy oil from Upper Cretaceous (Coniacian to Campanian) fractured dolomites. The second is the Deep Lacq reservoir, which is located at a depth of 3700m and is capped by the overlying early Aptian Sainte Suzanne marls (Figs 2 and 3) (Le Marrec et al., 1995). Here, Jurassic to Barremian limestones and dolomites produce mainly dry gas.

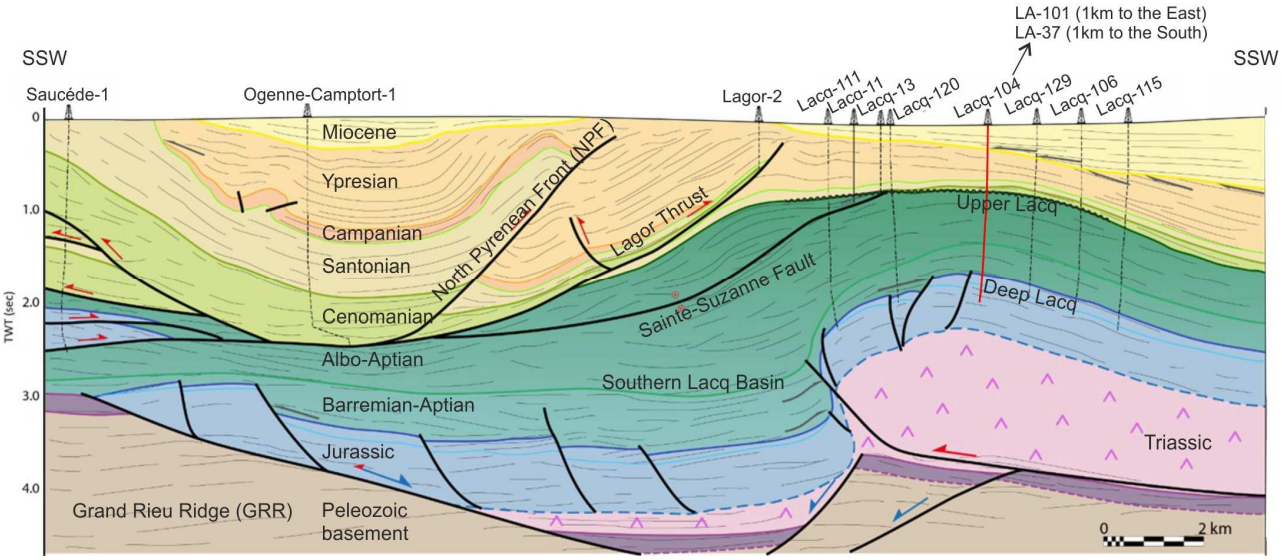

115

116 Figure 2. Interpreted NNE-SSW seismic cross-section through the Lacq structure in the
117 Arzacq basin (See Figure 1 for location). Due to the lack of a reliable velocity model the
118 vertical scale is in two-way time (TWT). For equivalent depth estimations, well LA-104 (red
119 line), reaches a true vertical depth (TVD) of 4346 m.

120

121 The structural and sedimentary history of the Lacq area is closely linked to the relative
122 motion between the Iberian and European plates during the Mesozoic and Cenozoic eras
123 that first generated the Arzacq rift basin and the subsequent Pyrenean orogeny and
124 associated Aquitaine foreland basin. Initial crustal architecture was partly inherited from
125 the Paleozoic Variscan orogeny (Kroner and Romer, 2013).

126 A simplified lithostratigraphic section of the southern Aquitaine basin with the timing of the
127 main geodynamic events are compiled in figure 3.

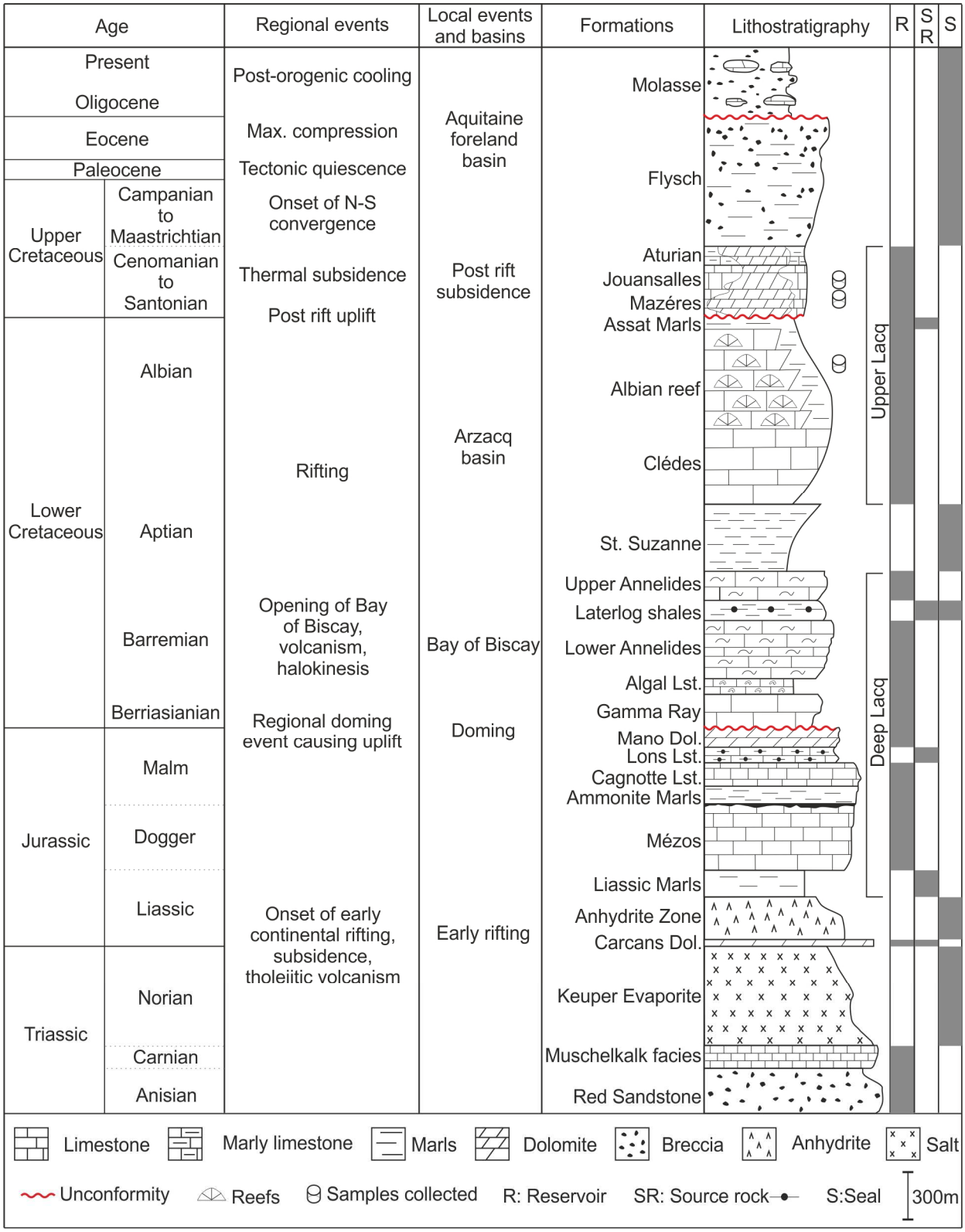

Figure 3. Lithostratigraphic column of the Arzacq and SW Aquitaine Basins including elements of the Lacq petroleum system and a summary of main geodynamic events, which impacted the area since the Triassic.

Triassic to Jurassic times marked the onset of continental rifting between the European and Iberian plates associated with the breakup of Pangea. Early rifting resulted in tholeiitic volcanism and evaporitic sedimentation (Bilotte et al., 2001; Biteau et al., 2006). Triassic formations consist of basal fluvial sandstones (Red sandstone), limestones and dolomites

(Muschelkalk) and evaporites (Keuper) (Lucas, 1985; Fréchengues et al., 1990; Le Marrec et al., 1995). The Lower Jurassic begins with the deposition of the Carcans Dolomites followed by the Liassic anhydrite unit (Curnelle et al., 1982; Curnelle and Dubois, 1986). The Middle Jurassic is represented by the clay-rich to peloidal limestones of the Mézos Formation (Canerot, 1991; Le Marrec et al., 1995). Upper Oxfordian Ammonite Marls cover a condensed ferruginous crust (Canérot et al., 1990) corresponding to the Callovo-Oxfordian subaerial exposure. During the Kimmeridgian, shelf carbonates were deposited (Cagnotte Formation) followed by the Lons Formation (Upper Kimmeridigan) consisting of marly limestones and dolomites, which is the main source rock for most of the petroleum systems in the Aquitaine basin (Connan and Lacrampe-Couloume, 1993; Le Marrec et al., 1995). The dolomitized oolitic limestones of the Mano Dolomite Formation (Fig. 3) represent the end of the Jurassic. During the Early Cretaceous the opening of the Bay of Biscay dissected the Aquitaine platform into two subsiding rifts: the Parentis basin to the north and the Arzacq basin to the south (Jammes et al., 2010). In the Arzacq basin the Hauterivian-Barrémien deposits are subdivided into four formations, from bottom to top (Fig. 3): Algal Limestones, Lower Annelids Limestones, Laterlog shales, and Upper Annelids Limestone Formations.

The Aptian records the onset of the main episode of rifting between the European and Iberian plates, characterized by an extreme crustal thinning leading to mantle exhumation (Clerc et al., 2015; Clerc and Lagabrielle, 2014; Jammes et al., 2010; Lagabrielle et al., 2010; Vacherat et al., 2016, 2014). Increased subsidence during the Early Aptian resulted in the deposition of 600 m of silty marls of the Sainte Suzanne Marl Formation (Biteau et al., 2006; Le Marrec et al., 1995). During the Middle Aptian, marly sediments of the Lower Cledes Formation were deposited while the Late Aptian to Late Albian is characterized by patch-reefs known as the Albian facies on the uplifted salt-cored Lacq structure (Biteau et al., 2006). The laterally equivalent and overlying Assat Marl Formation covered the entire basin (Fig. 3). Because of the crustal asymmetry at the base of the Mauléon and Arzacq

basins, Masini et al. (2014) distinguished a lower “plate” of the rift system and an upper plate separated by a detachment surface. The deformation migrated along the detachment surface between the Arzacq and Mauléon basins during the Albo-Aptian. Major faults developed in the lower plate and formed the Mauléon basin while passive sagging characterized the Arzacq basin on the upper plate section (Masini et al., 2014). The base Cenomanian is a regional unconformity, linked to the post rift uplift (Lagabrielle et al., 2010). The Cenomanian is marked by the deposition of shallow platform carbonates of the Mazéres Formation, constituting the main reservoir of Upper Lacq (Biteau et al., 2006). The micritic and rudist-bearing Jounsalles Formation represent the Coniacian to Early Campanian in the Lacq area. By the end Santonian the tectonic regime in the Pyrenean domain started to change with the onset of N-S closure of the exhumed mantle domain (Lagabrielle et al., 2010; Mouthereau et al., 2014; Plaziat, 1981; Teixell et al., 2016; Vacherat et al., 2014). All subsequent units were deposited in the Aquitaine foreland basin. The Middle and Upper Campanian is represented by the marly limestones of the Aturian Formation. The Paleocene to Eocene times recorded the deposition of the Flysch Formation characterized by debris flows, turbiditic conglomerates and marls (Puigdefabregas and Souquet, 1986). During the climax of convergence (Middle to Late Eocene), the entire Pyrenean chain emerged and supplied large volumes of detrital sediments to the southern Aquitaine basin (Jammes et al., 2009; Masini et al., 2014).

3 Material and methods

3.1 Sampling

The core samples from the Upper Lacq carbonate reservoir were collected from the well LA-37 (latitude: 43.411004° and longitude: -0.634984°, Fig 1 and 2). Given its location in the center of a square delimited by four oil-producing wells, LA-37 constitutes a suitable control well to study reservoir properties. It reached the water table at 723 m and crosscut the Coniacian to Campanian reservoirs. The sampling strategy focused on coarse cement phases, fractures, veins, stylolites and cross-cutting relationships observable at the

190 macroscopic scale. Initially, 358 thin sections, belonging to wells LA: 52-53-57-58-62-63-
191 69-80-84-1-10-101-36-4-37-104-102, were provided from TOTAL's archives. Public data
192 on these wells can be found at the French national geological survey website (BRGM:
193 infoterre.brgm.fr). After a preliminary evaluation on the thin sections, four wells were
194 selected (LA: 37-101-104 – Fig. 2), from which 88 new core samples were collected. The
195 samples most suitable for petrographic and chemical analyses were most retrieved from
196 the Jouansalles formation (Fig. 3).

197 3.2 Staining

198 Staining is a rapid technique to distinguish calcite, ferroan calcite, dolomite and ferroan
199 dolomite in thin sections. Preparation of the solution was performed following Dickson
200 (1965). The solution is composed of 3/5 of alizarin red solution and 2/5 of potassium
201 ferrycyanide solution. Half of thin sections were soaked for nearly 1 minute then rinsed
202 with distilled water and left to dry.

203 3.3 Petrography

204 16 facies were recognized using optical, cathodoluminescent and fluorescent
205 microscopes. Cold Cathodoluminescence (CCL) analysis was performed by using a
206 Cathodyne OPEA cold cathode instrument (400 mA and 13-15 kV gun current) in the
207 GeoRessources Laboratory (Nancy, France). Limestone descriptions were carried out by
208 using the classifications of Folk (1962) and Dunham (1962). Porosity description was
209 based on the classification of Choquette and Pray (1970). Calcite textures and growth
210 habits were based on the scheme of Flügel (2004) whereas dolomite textures were
211 described according to Sibley and Gregg (1987).

212 3.4 Isotope Geochemistry

213 3.4.1 Carbon, Oxygen and clumped isotope analysis ($\delta^{18}O$, $\delta^{13}C$ and Δ_{47})

214 Conventional $\delta^{18}O$ and $\delta^{13}C$ analysis were performed on 36 powder samples collected
215 with a DREMEL micro-drill on samples not impregnated by resin. Special care was taken

to avoid risks of mixing several generations of cement. A Thermo Scientific MAT253 isotope ratio mass spectrometer at the CRPG laboratory (Nancy France) was used to perform $\delta^{18}O$ and $\delta^{13}C$ analyses. Measurements were calibrated using international standards IAEA CO-1, IAEA CO-8 and NBS 19. Reproducibility was checked by replicate analysis of laboratory standards and was ±0.07‰ (1SD, n=14) for oxygen isotopes and ±0.02‰ (1SD, n=14) for carbon isotopes. A subset of 8 samples was later selected for clumped isotope thermometry investigation. Δ_{47} measurements have been performed at California Institute of Technology (USA) with an automated acid digestion and gas purification device coupled to a dual inlet Thermo MAT253 as described in Passey et al. (2010). Samples weighed into silver capsules (~ 8 mg) were reacted in a common phosphoric acid bath (~103 %) for 20 minutes at 90°C under static vacuum (evacuated to <0.5 Torr at the beginning of the reaction). The evolved CO_2 was passed through an ethanol/dry ice U-trap (~ -80°C) before being collected on a liquid nitrogen temperature (-196°C) U-trap. Following the 20 minutes reaction period, the CO_2 was carried through a Porapak Q 120/80 mesh gas column held at -20°C using He as the carrier gas. The purified CO_2 was analyzed using a Thermo Scientific MAT 253 Mass Spectrometer configured to collect masses 44–49. Mass 48 was monitored to detect any hydrocarbon contamination. Measurements of each gas were done at 16 V of mass 44 and consisted of 8 acquisitions, each of which involved 7 cycles of sample-standard comparison with an ion integration time of 26 s per cycle (i.e., total integration time of 1456 seconds for each CO_2 sample).

$\delta^{18}O$ and $\delta^{13}C$ data were also acquired as part of each Δ_{47} analysis and were calculated using the “Brand” parameters reported in Brand et al. (2010). In order to account for the temperature dependence of oxygen isotope fractionation between CO_2 gas and carbonate resulting from the reaction with phosphoric acid at 90°C, fractionation factors of 1.00811 and 1.009218 were used for calcite and dolomite respectively following Rosenbaum and Sheppard, (1986) and Swart et al. (1991). The Δ_{47} raw data were corrected for instrument

243 nonlinearity and scale compression (Huntington et al., 2009; Passey et al., 2010). Several
244 heated (at 1000°C) and equilibrated gases (at 25°C) of various bulk isotopic compositions
245 were run during each session. These gases were used to convert measurements into the
246 interlaboratory absolute reference frame (Dennis et al., 2011). $\delta^{18}O$ and $\delta^{13}C$ values are
247 expressed in per mil with respect to the VPDB standard. To guarantee accuracy of the Δ_{47}
248 data, we routinely analyzed two carbonate reference materials (Carrara marble and TV04,
249 also reported by Dennis et al., 2011 and many other studies). One of these two carbonate
250 standards was analyzed typically every five analyses and distributed along the diagenetic
251 cement samples in order to check for analytical stability/accuracy of the whole procedure,
252 as well as long-term external reproducibility of our measurements. The Δ_{47} values
253 obtained are: $\Delta_{47\text{-CDES25}}$ = 0.409 ± 0.019‰ (1SD, n = 19) for Carrara; $\Delta_{47\text{-CDES25}}$ = 0.670 ±
254 0.014‰ (1SD, n =16) for TV04.

255 Finally, the corrected Δ_{47} values were converted into temperatures using the composite
256 Δ_{47}-T calibration determined for all carbonate minerals for the 0–300°C temperature range
257 (i.e. Bonifacie et al. (2017); $\Delta_{47\text{-CDES90}} = 0.0422 \times 10^6 / T^2 + 0.1262$). The oxygen isotopic
258 compositions of the water ($\delta^{18}O_{water}$) from which the carbonates precipitated were
259 calculated for each estimated $T\Delta_{47}$ using the $\delta^{18}O_{carb}$ values measured for the carbonate
260 as well as the oxygen isotope fractionation between the carbonate and water from O'Neil
261 et al. (1969) for calcite and Horita (2014) for dolomite.

262 3.4.2 Multiple Sulfur isotopes analysis

263 Multiple sulfur isotopes analysis ($\delta^{34}S$, $\delta^{33}S$, $\delta^{36}S$) was performed on carbonate-associated
264 sulphate (CAS) on anhydrite-rich samples from the LA-37 well. The extraction technique of
265 Sansjofre et al. (2016) was used to analyze CAS isotopic signature. This technique
266 involves leaching the soluble sulfates fraction with saline water several times before
267 dissolving the carbonates in 4N HCl solution over 12 hours. Then, a solution of $BaCl_2$ was
268 added to the acidified sample to precipitate sulfates as barium sulfates.

The recovered barium sulfates were reacted with the Strongly Reducing Hydriodic Hypophosphorous acid solution (STRIP) (Kitayama et al., 2017) to produce Ag_2S upon reacting with $AgNO_3$ solution. This Ag_2S is then reacted with F_2 during a whole night in nickel containers at 350°C to produce SF_6. After cryogenic and gas chromatography separation steps, the resulting SF_6 was analyzed in a ThermoFinnigan MAT 253 dual-inlet gas-source mass spectrometer. All the different steps of the multiple sulfur isotopes analysis were carried out at the Institut de Physique du Globe de Paris (IPGP, France). Values are given with respect to Vienna Cañon Diablo Troilite (V-CDT) related to the classical delta notation.

3.5 LA-ICPMS

Laser Ablation-Inductively Coupled Mass Spectrometry (LA-ICPMS) was used to study Rare Earth Elements (REE) in dolomite and calcite cements and to check if these samples match the prerequisite U and Pb content needed for absolute age dating. The analyses were carried out at the GeoRessources laboratory in Nancy. Laser sampling was performed with a 193 nm GeoLas Pro ArF Excimer laser (Microlas®, Göttingen, Germany) equipped with beam homogenization optics. Ablation was performed by focusing the beam at the sample surface with a constant fluency of 10 J/cm^2 and constant repetition rate of 5 Hz. Helium was used as a carrier gas to transport the laser generated aerosols from the ablation cell to the ICP-MS. Ablated material was analyzed by an Agilent 7500c Quadrupole ICP-MS (Agilent®, Santa Clara, California) equipped with an Octopole Reaction System with enhanced sensitivity optional lenses (Cs type, Agilent). The certified glass standards NIST610, NIST612 and NIST614 SRM were used as reference materials. Detection limits range from a few ppm for Ce to 0.5 ppm for heavy rare earth elements. For consistent representation, the REE concentrations obtained were normalized to the Post-Archean Australian Shale (PAAS).

3.6 Fluid Inclusion Microthermometry

295 Microthermometric measurements were performed on a Linkam THMS600 heating-
296 cooling stage connected to an Olympus BX51 microscope (GeoRessources, Nancy,
297 France). The stage was calibrated using synthetic H_2O pure fluid inclusion standard and a
298 natural aqueous fluid inclusion standard (Ta 33.2) with the following phase transitions: ice
299 melting (T_m ice) at 0.0°C, homogenization temperatures (T_h) at 164.0°C and eutectic point
300 of H_2O-NaCl at -21.2°C. The acquired temperatures of phase transition (i.e.
301 homogenization into the liquid phase) have an accuracy of about ±0.2°C, and the obtained
302 data were calibrated accordingly. In the case of fluid inclusions trapped in dolomites, the
303 glass cover of the stage was removed to allow clearer observations of the very small
304 inclusions. Without the glass cover, the error range increased to +1.6°C.

305 3.7 Raman Spectroscopy

306 Raman spectroscopy was used to determine the composition of gas phases in aqueous
307 fluid inclusions following the procedure outlined in Caumon et al. (2015). Analyses were
308 performed with a LabRAM HR spectrometer (Horiba Jobin Yvon) equipped with a 600
309 $g.mm^{-1}$ grating and an Edge filter. The confocal hole aperture was 500 µm and the slit
310 aperture was of 200 µm. The excitation beam was provided by a Stabilite 2017 Arþ laser
311 at 457.9 nm or 514.5 nm and a power of 200 mW, implying a power of 20 mW on the
312 sample. The acquisition time was 10 s and the number of accumulations was 10 in order
313 to optimize the signal-to-noise ratio.

314 3.8 Fourier Transform – Infrared Spectroscopy (FT-IR)

315 FT-IR was used to identify possible compositional differences between the different types
316 of oil inclusions. Infrared spectra were recorded with a Bruker Fourier Transform Infrared
317 (FTIR) spectrometer Equinox 55, coupled with a Bruker A590 microscope. The microscope
318 is equipped with a narrow-band mecury-cadmium-telluride (MCT) detector with a 100 µm
319 diameter window, cooled to 77 K. The spectra were obtained in transmission mode in the
320 mid infrared range (4000-400 cm^{-1}) with a 4 cm^{-1} spectral resolution. A series of circular
321 diaphragms allowed the diameter of the analyzed section to vary from 100 to 20 µm with

322 the objective magnification of X15. µFTIR spectra were obtained in less than 2 minutes by
323 the accumulation of 200 scans.

324 3.9 Confocal Scanning Laser Microscopy (CSLM)

325 For pressure-temperature modeling, it is necessary to consider the volume percentage of
326 the gas phase with respect to the oil volume and the temperature. This was obtained using
327 a CSLM fitted with a Biorad Rainbow system adapted to a Nikon inverted microscope at
328 the GeoRessources Lab (Nancy, France). The emission source was an Argon laser at 488
329 nm and a diode laser at 405 nm. The objective had an oil immersion 60x lens. This method
330 allows the gas volume percentage of the petroleum inclusion to be determined with an
331 accuracy greater than 95 %. The x–y resolution is 0.2 µm and the resolution along the z-
332 axis is approximately 0.5 µm. The studied chips were glued onto a glass plate using
333 paraffin to avoid any movement during acquisition. For better accuracy, the radii of the gas
334 phases in oil inclusions were measured prior to CSLM measurements using optical light
335 microscopes.

336 3.10 Image processing

337 To perform volumetric calculations, the slices of the 3D image obtained through CSLM
338 were processed to remove any polluting fluorescence from nearby objects. This was done
339 through ImageJ software. First, the greyscale histogram of the images was plotted with MS
340 Excel and its 6^{th} degree best-fit polynomial equation (R = 0.95 - 0.99) was obtained. Using
341 MatLab, the second derivative was then obtained and the solution for f”(x) = 0 was used as
342 the maximum threshold limit in ImageJ. This procedure objectively and systematically
343 cleared the noisy fluorescence to calculate the gas volume, following the steps outlined in
344 Pironon et al., (1998).

345 3.11 Basin modeling

346 The Petromod 1D software was used to model the evolution of lithostatic and hydrostatic
347 P-T conditions over time. Stratigraphic and thermal maturity data were inserted into the

348 software to better constrain the basin model. True vertical depths (TVD) from well logs
349 were used as stratigraphic thicknesses of the drilled formations. Ages were determined
350 following the stratigraphic chart of Biteau et al. (2006), while the duration of unconformities
351 was deduced from Le Marrec et al. (1995), Bilotte et al. (2001) and Huyghe et al. (2012).
352 The total subsidence evolution was obtained by using the backstripping method. The
353 amount of eroded material associated with unconformities was estimated on the basis of
354 the best-fit scenario between the measured and simulated vitrinite maturities.

355 Drilling reports during the operations of wells LA-101-104-37-36 provided data about
356 porosity, permeability and density, which were added as calibrations to Petromod 1D.
357 Also, organic geochemistry data involving RockEval results (TOC, S1, S2, S3 and Tmax)
358 were collected from unpublished internal TOTAL reports and added as thermal
359 calibrations. Source-rock typing by Connan and Lacrampe-Couloume (1993) provide
360 suitable biomarker data (sterane isomerization: 29ααS/29ααR) to calibrate source rock
361 maturity.

362 # 4 Results

363 ## 4.1 Petrography of diagenetic phases

364 ### 4.1.1 Host Rock

365 Host rocks in Upper Lacq consists of intramicrite to biomicrite facies (Folk, 1962) with a
366 wackestone to packestone texture (Dunham, 1962) (Fig. 4a). Skeletal fragments of
367 foraminifera, echinoderms, and gastropods are abundant and can reach up to 700 µm in
368 length. The red color after staining indicates a non-ferroan composition of the matrix. CCL
369 microscopy reveals a brown to dull-orange luminescence of the matrix.

370 ### 4.1.2 Glauconite

371 Pellets of glauconite have simple, rounded morphologies, with generally smooth surfaces
372 (Fig. 4a). Sizes range between 20 µm up to 200 µm. Rarely, some pellets are

amalgamated into larger aggregates. Local concentrations of glauconite are observed associated with stylolite residues.

4.1.3 Micrite rims

A few µm-thick rims of micrite penetrating some skeletal fragments were observed (Fig. 4c). These have a dark grey color in plane polarized light (PPL) and a bright yellow luminescence under CCL.

4.1.4 Framboidal pyrites

This phase of pyrite occurs as framboidal aggregates adjacent to shells and skeletal fragments. Under reflected light, pyrites appear as golden to bright yellow (Fig. 4d). Crystal sizes can reach up to 55 µm with rounded to sub-rounded geometries.

4.1.5 Chert Nodules

This scarce phase was observed only in a few samples. Individual nodules can reach up to 4 cm in length with circular to oblate morphologies. In thin sections, a few silica microfractures, with thicknesses of 2-4 µm can be seen cross-cutting or terminating at the chert nodules (Fig. 4e). Silica crystals have a white to yellowish grey color with sweeping extinction under cross-polarized light.

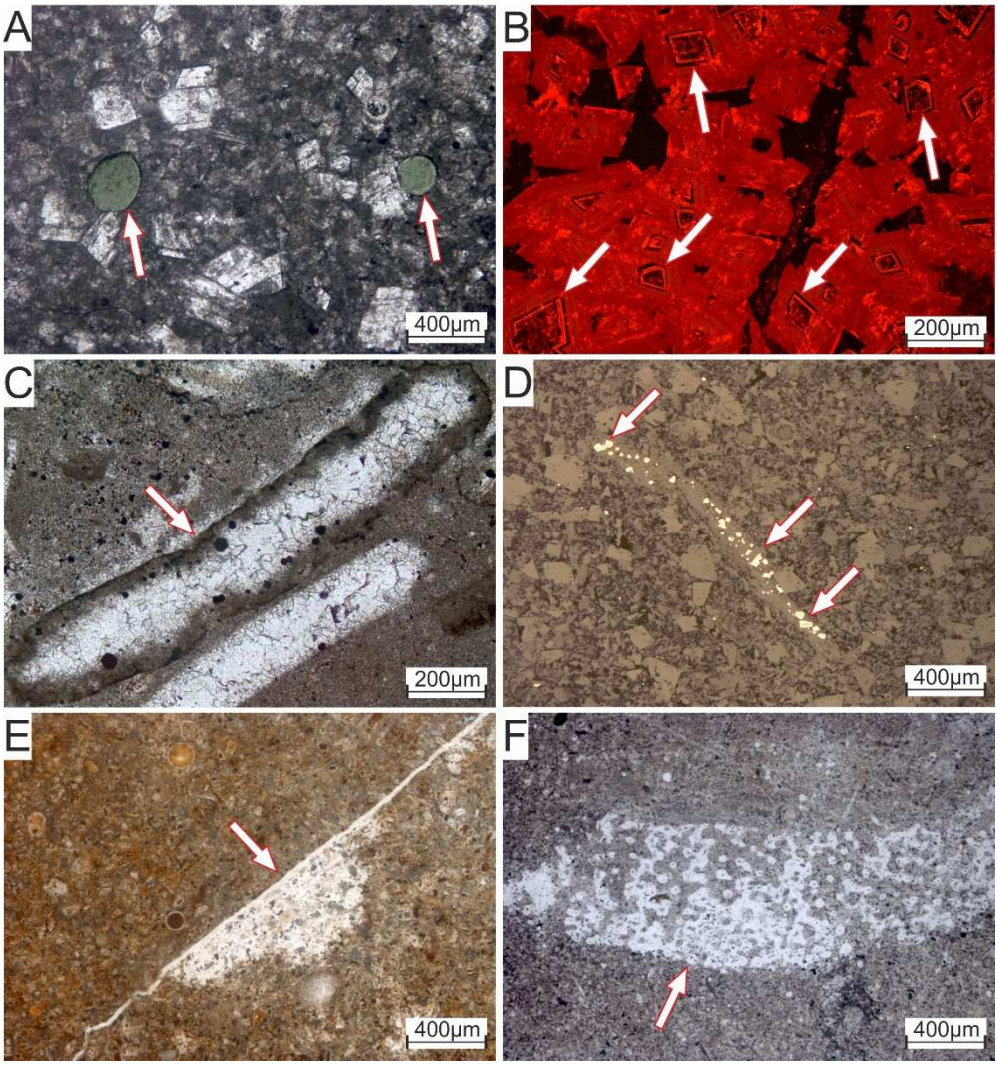

Figure 4. A: Limestone matrix with micrite and dolomite in PPL. Arrows point to the rounded greenish detrital glauconite pellets. B: CCL photomicrograph showing the dark zoned core of the D1 dolomite (arrows). The red-luminescent overgrowth corresponds to the D2 dolomite. C: Micrite rim (arrow) penetrating a shell fragment in PPL. D: Aggregates of bright yellow framboidal pyrite (arrows) inside in a bivalve shell in PPL. E: Microfracture (arrow) filled by silica in contact with a displaced chert nodule (in PPL). F: Clast of siliceous sponge (in PPL).

4.1.6 Dolomite D1

This phase consists of euhedral dolomite rhombs. They constitute the cores of dolomite crystals present in the matrix (Fig. 4b). Rhombs have average sizes between 30 and 200µm. Under PPL, D1 appears as turbid and rich in impurities. Fluid inclusions are too small to allow measurements. Under CCL, D1 is mostly non-luminescent with a single brightly luminescent rim. This phase is colorless after staining indicating a non-ferroan composition.

4.1.7 Pyrite 2

405 The second phase of pyrites appear as cubes larger than the early framboidal aggregates.
406 Individual crystal sizes can reach up to 2.5 mm in length (Fig. 5a). In some cases, relics of
407 dolomite rhombs were observed inside the engulfing pyrite crystals. No cross-cutting
408 relationships with the later dolomite/calcite phases were observed and thus its timing
409 cannot be robustly determined.

410 4.1.8 Fracture (breccia)

411 Brecciated fragments of D1 were observed under PPL. Under CCL, edges of brecciated
412 crystals show an irregular non-planar shape and a bright yellow external rim probably due
413 to a dissolution event (Figs. 5b and 5c).

414 4.1.9 Saddle Dolomite D2

415 This phase has two morphologies. The first engulfs D1 cores and appears as creamy
416 white overgrowth cement under PPL and labeled D2. When viewed under CCL, a uniform
417 bright red luminescence was observed (Figs. 4b and 5b). Overgrowths can reach up to
418 150 µm in thickness and contain some aqueous fluid inclusions that were investigated in
419 this study. The non-ferroan composition of D2 is attested by its white color after staining. In
420 fractures (Fig. 5b) or in mm-scale vuggy porosity, coarse dolomite crystals were observed.
421 The latter morphology is that of the saddle dolomite crystals. Under cross-polarized light,
422 crystals show typical sweep extinction. CCL observations revealed a uniform bright red
423 luminescence. Crystal sizes can reach up to 2 mm in length. Similarly, colorless results
424 after staining indicate a non-ferroan composition. This dolomite phase was not affected by
425 brecciation (Fig. 5b), but was impacted by stylolites (Fig. 5c).

426 4.1.10 Stylolites

427 Stylolites affect the brecciated D1 and the saddle dolomites (Fig. 5c). The oblique direction
428 of stylolite peaks in vertical wells indicates that they are tectonic in origin and formed
429 during Pyrenean shortening. Concentrations of glauconite along stylolites have also locally
430 been observed. In a few thin sections, the amplitude of stylolites can reach few mm.

4.1.11 Fracture and dissolution

Fractures with open pore spaces cross-cut the host rocks. The width of open fractures can reach 4-6 mm. Blocky calcites are often observed on the edges of fractures (Fig. 5e and f). Dissolution is mostly expressed through the partial dissolution of stylolites (Fig. 5d) and the partially eroded walls of the calcite-infilled fractures (Fig. 5e and f).

4.1.12 Blocky Calcites

This cement phase is creamy white to transparent in PPL with typical cleavage planes at 74° and 55°. Growth habits include equant to blocky forms with larger crystal sizes towards the center of pores and fractures (Fig. 5e). Individual crystal sizes can reach up to 3 mm. CCL microscopy revealed a dark brown to dull orange luminescence (Fig. 5e). These calcites are the main pore-reducing cements and occlude most of the inter-dolomite and fracture porosity. The pink color after staining indicates a non-ferroan composition (Fig. 5d).

4.1.13 Oil emplacement

Oil inclusions exist inside the blocky calcite and oil coatings occur on calcite and dolomite crystals. Oil inclusions have a brown to orange color under ultraviolet (UV) light, while the coatings on calcites show a darker brown color (Fig. 5f).

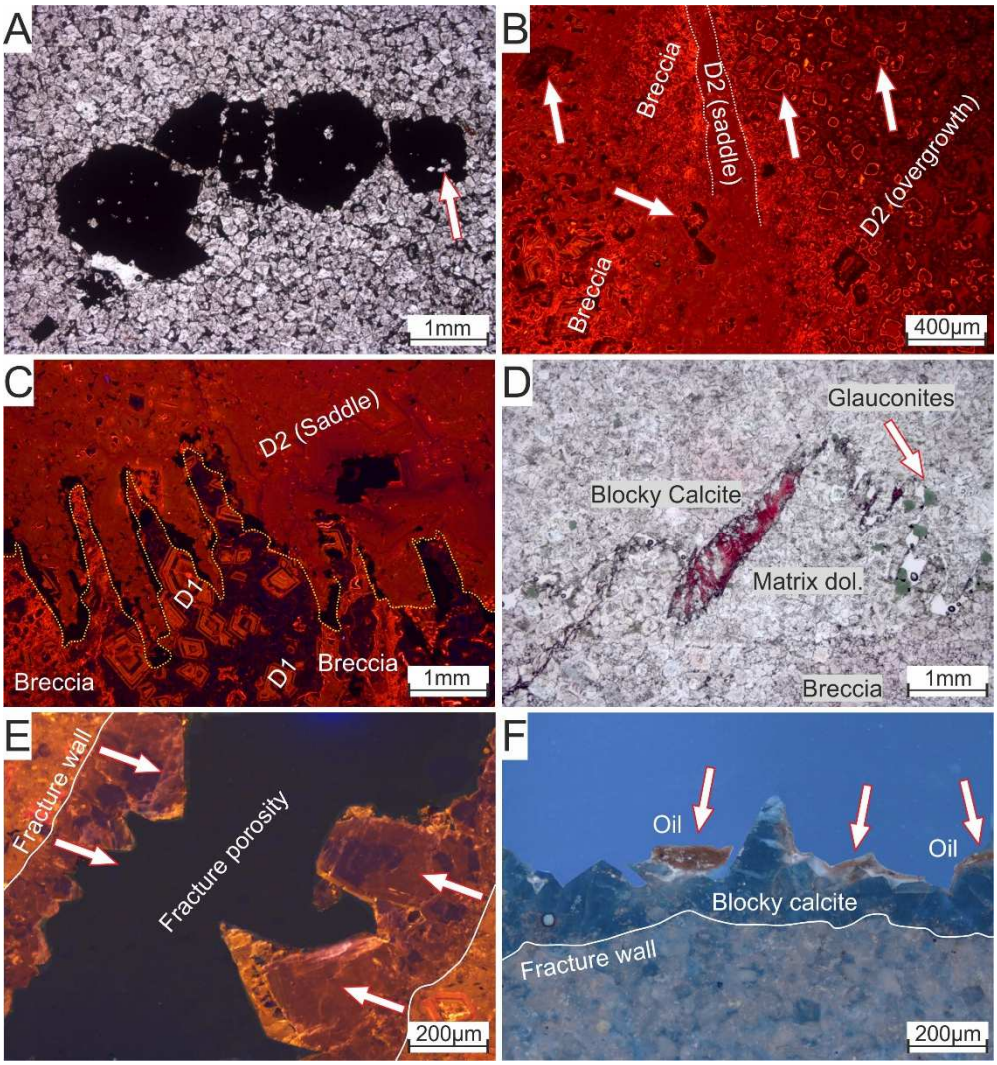

Figure 5. A: Pyrite 2 crystals engulfing some relics of dolomites (arrow; in PPL). B: CCL Cross-cutting relationships between fractures (between dashed line), partially dissolved and brecciated D1 rhombs (arrows) engulfed by the D2 overgrowths. C: CCL image of a stylolite (yellow line) impacting both brecciated D1 dolomites and saddle dolomites D2. D: Partially dissolved stylolite, in dolomite matrix, filled with pink-stained, blocky calcite (in PPL). Glauconites (arrow) are also displaced and concentrated along the stylolite surface. E: CCL image of fracture walls lined with dull orange to brown blocky calcites. The crystal size increases towards the center of the fracture as indicated by the arrows. F: Same fracture under UV light with oil coatings (arrows) on top of the blocky calcites.

4.1.14 Anhydrite

A few creamy white to colorless tabular crystals of anhydrite constitute the last diagenetic phase in the sequence. They are identified by their bright 2nd order birefringence colors under crossed-polars (Fig. 6a). Cleavage plans are parallel to the main growth axis. These anhydrites post-date calcite cements and contain no aqueous or oil inclusions.

4.1.15 Groundwater

Present-day operators of the Lacq field report the existence of the watertable at a depth of nearly 723 m. Ground water is thus added to the paragenesis as a separate phase.

4.1.16 Iron Oxides

This scarce phase is represented by brown to orange coatings surrounding a few pyrite crystals (Fig. 6b). Under reflected light, the coatings appear dark brown to black. The pyrites engulfed by the iron oxides show non-planar and altered crystal edges.

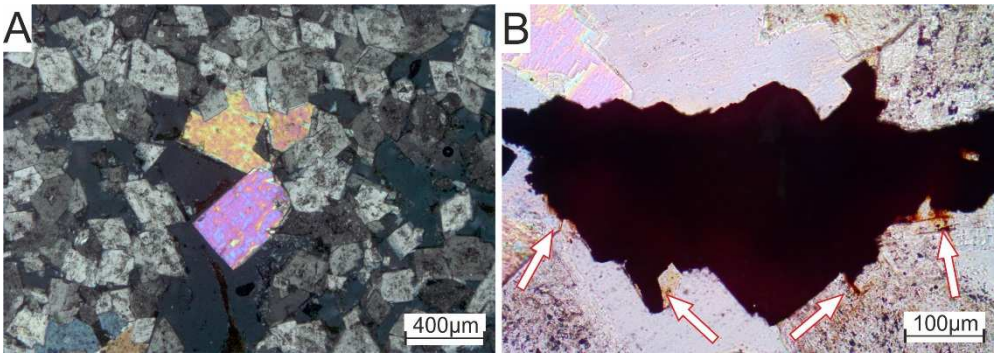

Figure 6. A: Tabular anhydrite crystals under cross-polarized light showing typical 2nd order birefringence colors. B: Iron oxides (arrows) on the edges of a pyrite crystal. The colored crystal on the left corner is a tabular anhydrite.

4.2 Fluid Inclusion Studies

4.2.1 Petrography

Phases of interest with abundant aqueous inclusions are the D2 overgrowths, saddle dolomites and blocky calcites (Fig. 7). Fluid inclusions in the D2 dolomites (Fig. 7a) have two phases (liquid and gas) with rectangular to oval shapes and average sizes around 5-8 µm (Fig. 7b). Similarly, in the saddle dolomites, two phases of aqueous inclusions were identified in growth zones (Fig. 7c) and have rectangular to elongated shapes with sizes between 5 and 10 µm (Fig.7d). The two-phase aqueous inclusions in blocky calcites (Fig. 7e) are larger, reaching up to 20 µm in size and with shapes ranging from geometric (rectangular, cubic and triangular) to lozenge and oblate (Fig. 7f).

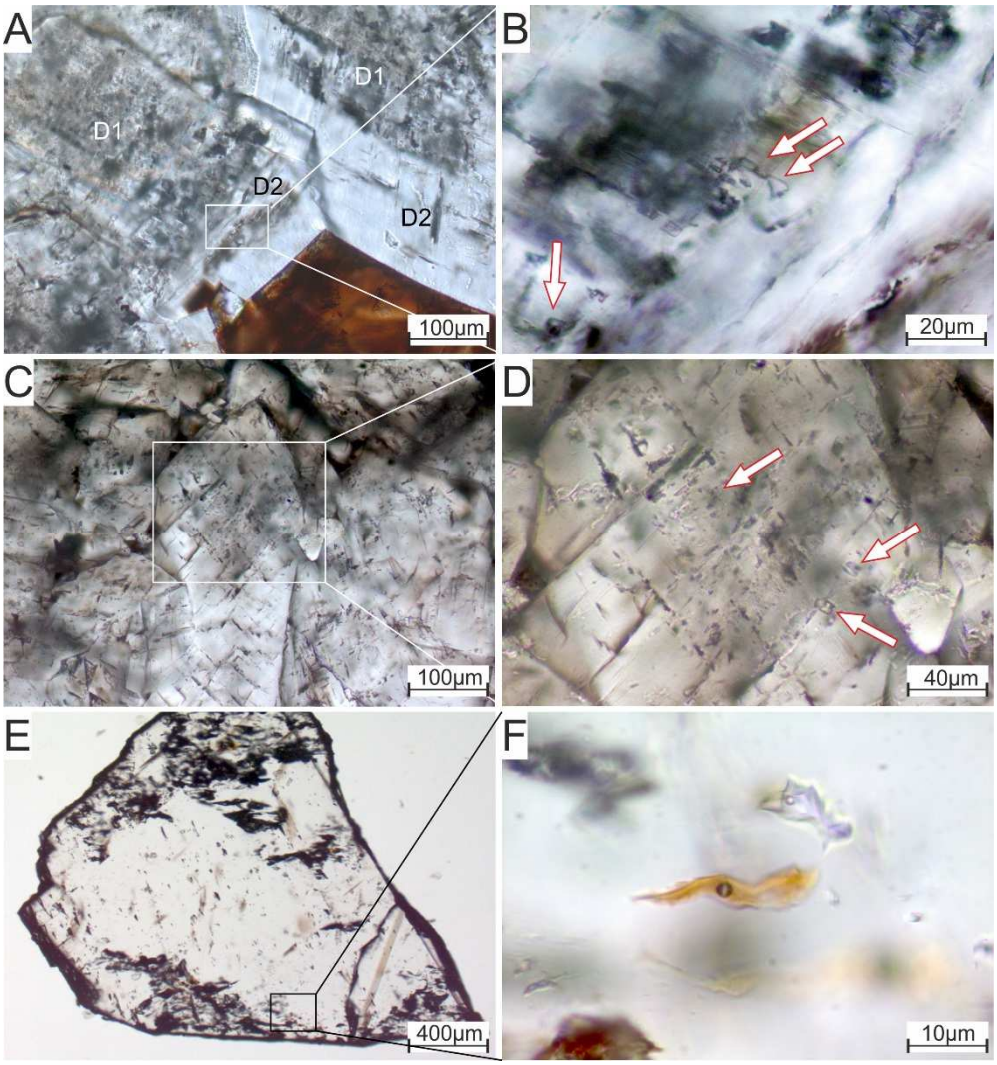

Figure 7. A: D2 overgrowth around D1 cores. B: Zoom of the image A showing two-phase aqueous inclusions (arrows) in D2. C: Large crystals of saddle dolomite with their typically curved edges. D: Zoom of the image C with rectangular two-phase aqueous inclusions (arrows). E: Crystal of blocky calcite containing patches of oil and aqueous inclusions. F: Zoom of the image E showing two-phase oil (orange) and aqueous (clear) inclusions.

Two types of oil inclusions occur in the blocky calcite of Upper Lacq. Under UV, the first type has a brown fluorescence, while the second type shows a strong white fluorescence. Both types of oil inclusions were observed very close to aqueous inclusions in the blocky calcite (Fig. 7f) and are absent from the D2 or saddle dolomite phases. This co-genetic association of oil and aqueous inclusions, and their absence in older diagenetic cements indicate that oil inclusions are primary.

4.2.2 Fourier Transform – Infrared Spectroscopy (FT-IR).

497 Hydrocarbons with a brown fluorescence are characterized by a spectrum suggesting the
498 occurrence of water and aromatics, which are absent in the inclusions with strong white
499 fluorescence. Both types of hydrocarbons have very low CH_4 content.

500 4.2.3 Microthermometry

501 Microthermometry data were obtained from fluid inclusions (FIs) in D2 overgrowths, saddle
502 dolomites (Fig. 8a) and calcite phases (Fig. 8b). Because D2 and saddle dolomites are
503 considered as different morphologies of the same phase, their FI data are joined together.
504 All FIs in all the studied phases homogenized into the liquid phase, i.e. disappearance of
505 the gas phase at T_h. FIs in D2 and saddle dolomites homogenized at a T_h mode ranging
506 between 77 and 80°C. (Fig. 8a). T_h values for blocky calcites show a more restricted mode
507 around 76 and 80°C (Fig. 8b). Oil inclusions with brown fluorescence in blocky calcites
508 have T_h values between 56°C and 68°C with a T_h mode around 66-68°C. Oil inclusions
509 with white fluorescence are rare and homogenize at around 70°C (Fig. 8b).

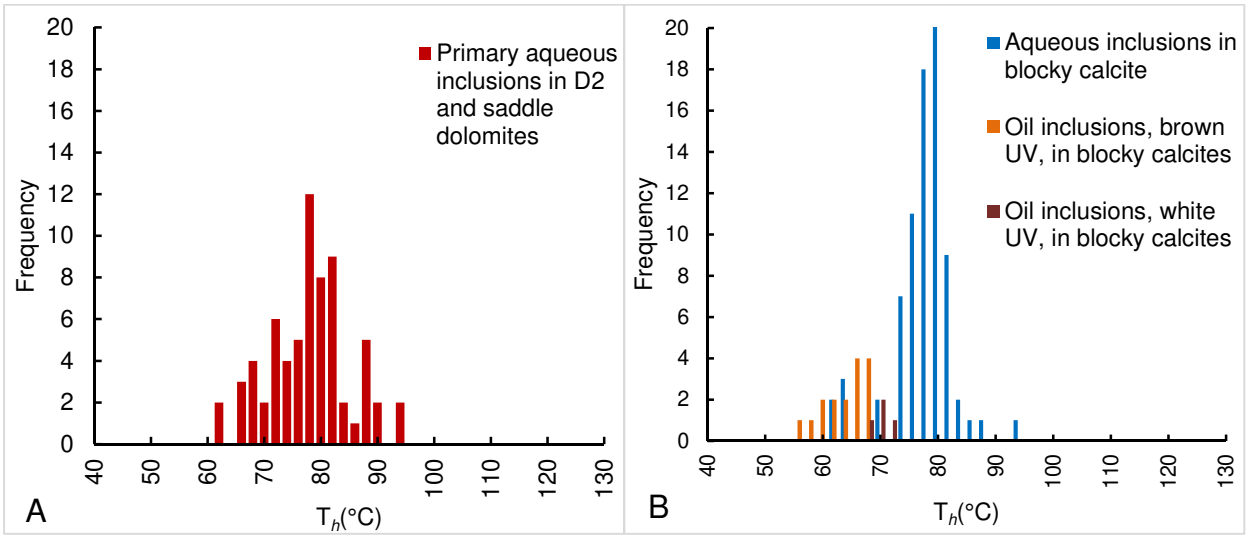

510

511 Figure 8: Frequency histograms of the homogenization temperatures of aqueous and oil
512 inclusions in (A) dolomite and (B) calcite phases.

513 In the Albian reefs (Fig. 3) at depths of 1400-1403 m, the main inclusion type trapped in
514 the blocky calcite phase is a brown-fluorescent oil homogenizing at around 76-80°C (Fig.
515 9a). Aqueous inclusions are very rare but homogenize in the same temperature range as
516 the oil inclusions. After freezing down to -100°C, phase changes were observed, and final
517 ice melting temperatures were recorded. Eutectic (T_e) or first-melting temperatures were

difficult to record in most FIs, but in a few inclusions, first melting of ice with coexistence of solid (ice), liquid, and gas phases occurred between T_e of -21 to -22°C. Final ice melting temperatures were measured between -4 and -0.2°C. These values correspond to very low salinities, equal or lower than values of seawater (Fig. 9b).

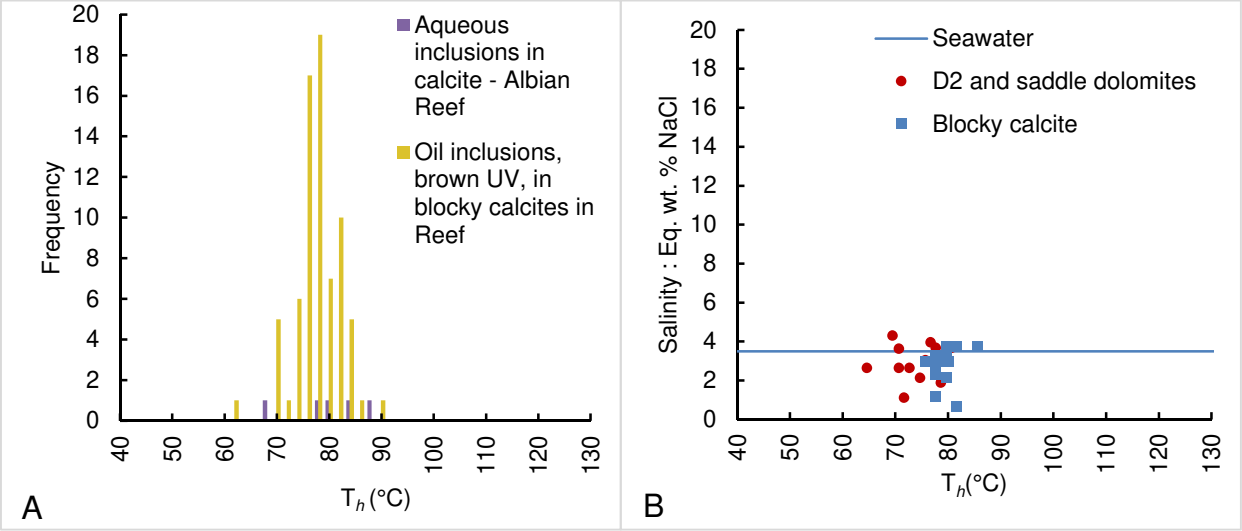

Figure 9: (A) Frequency histogram of homogenization temperatures of aqueous and oil inclusions in the blocky calcite of the Albian Reef Formation (Fig. 3). B: T_h vs. salinity cross-plot of the studied phases.

4.2.4 Raman Spectroscopy

The very low salinities measured with microthermometry were confirmed by Raman spectroscopy. Analysis of the liquid phase in fluid inclusions of the blocky calcite reveal salinities ranging between 1.2-2.4 % eq. wt. NaCl. These values are in the same range that those obtained through microthermometry. Raman measurements made on the gas phases showed no CO_2, CH_4, H_2S or any other gas component except H_2O vapor. Unfortunately, high fluorescence in dolomites prevented the acquisition of reliable data.

4.3 Isotope Geochemistry

$\delta^{18}O$ and $\delta^{13}C$ composition were measured in four different carbonate phases : (1) the host rocks (n=3), (2) the dolomitized matrix constituted by a mixture of D1 and D2 dolomites (n=28), (3) saddle dolomites (n=6) and (4) the final blocky calcite (n=6 ; Fig. 10). A few sub-samples from each carbonate phase were further investigated by carbonate clumped isotope thermometry (Δ_{47}). Figure 10 and Table 1 report the average $\delta^{18}O_{carb}$,

539 $\delta^{13}C_{carb}$, Δ_{47}, $T(\Delta_{47})$ and $\delta^{18}O_{water}$ results. The investigated carbonate rock has a "bulk"
540 $\delta^{13}C$ values ranging from -1.48‰ to 3.56‰ (VPDB) and $\delta^{18}O$ ranging from -2.25‰ to -
541 12.38‰ (VPDB). However, the genetically distinct phases show more homogeneous and
542 clustered $\delta^{18}O/\delta^{13}C$ values, with respective $\delta^{18}O$ composition of -3.44±0.79‰ for the host
543 rock, -5.34±1.23‰ for the dolomitized matrix, -8.72 ± 0.42‰ for the saddle dolomite and -
544 10.58 ± 1.08‰ for the last blocky calcite. Average $\delta^{13}C$ values are of 2.19 ± 0.92‰ for the
545 host rock, 2.96 ± 0.29‰ for the dolomitized matrix, 2.02 ± 0.80‰ for the saddle dolomite,
546 and 0.27 ± 1.10‰ for the blocky calcite. The $\delta^{18}O$ and $\delta^{13}C$ composition of the host rock
547 fall within the range of expected values for biogenic calcites precipitated in equilibrium with
548 Late Cretaceous seawater (Steuber, 1999). In contrast, the younger carbonate phases
549 show a gradual depletion in $\delta^{18}O$ and $\delta^{13}C$.

550 Similarly, each carbonate phase displayed distinctive Δ_{47} compositions convertible into
551 precipitation temperature estimations. Values obtained are of (1) 19 ± 5°C and 18 ± 15°C
552 for the host rock, (2) 58 ± 7°C, 63 ± 2°C and 56 ± 7°C for the dolomitized matrix samples,
553 (3) 92°C (error unknown as only one measurement) for the saddle dolomite and (4) 76 ±
554 5°C, 81 ± 6°C for the blocky calcite. As illustrated in figure 10b, the decrease in $\delta^{18}O$
555 values is correlated with an increase in Δ_{47} temperatures. The calculated oxygen isotopic
556 compositions of the parent fluids ($\delta^{18}O_{water}$) are of -1.9 to -1.7‰ SMOW for the host-rock, -
557 1.6 to +1.2‰ SMOW for the dolomitized matrix, -0.6‰ SMOW for the saddle dolomite and
558 +0.4 to +0.8‰ for the blocky calcite.

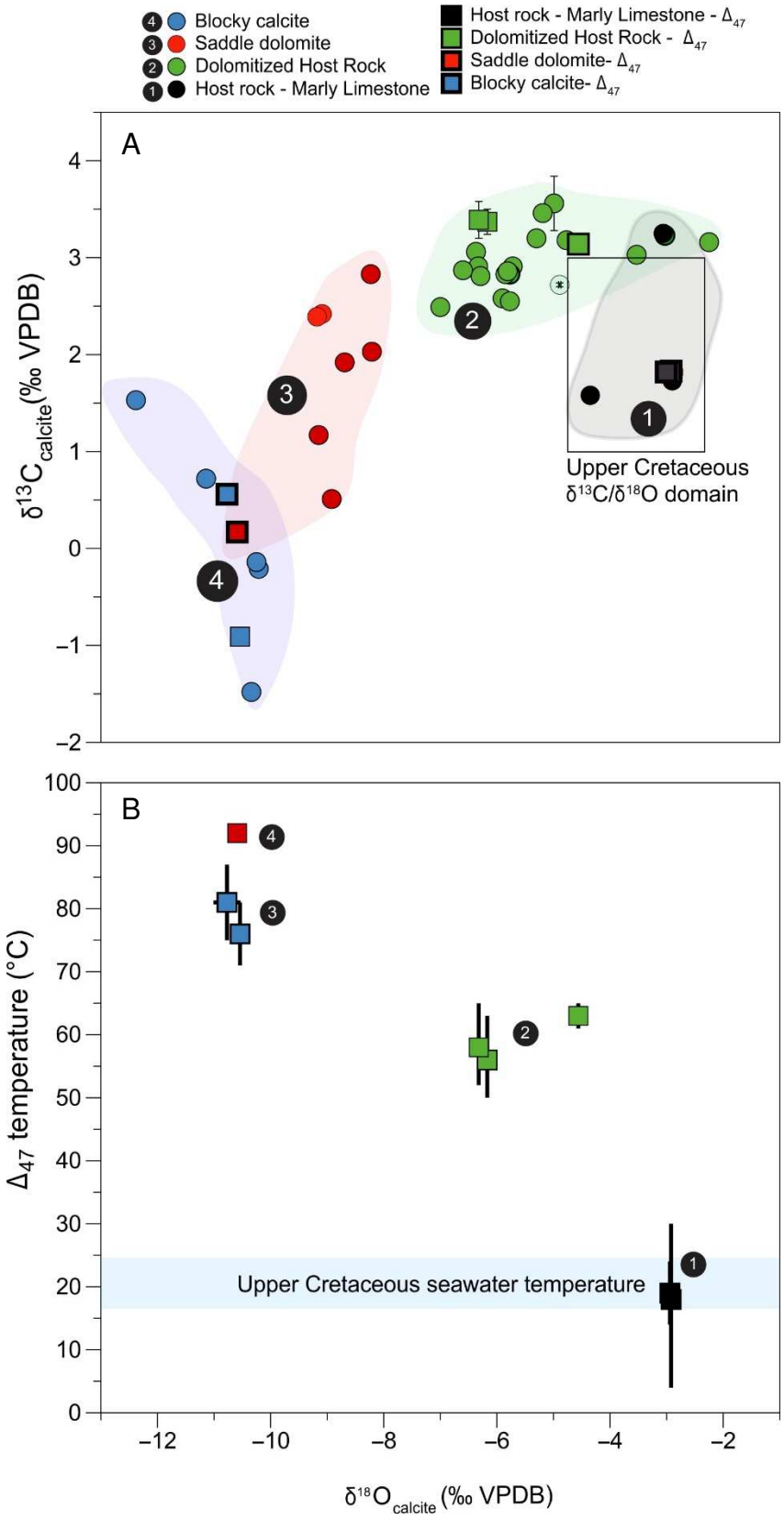

559

560 Figure 10. A: $\delta^{18}O/\delta^{13}C$ cross plot. Symbol colors refer to specific carbonate phases
561 numbered from '1' to '4'. The colored areas highlight the dispersion of $\delta^{18}O$ and $\delta^{13}C$
562 values recorded for each carbonate phase. Square symbol represents the sample selected
563 for clumped isotope measurements. When not shown, uncertainties are included in the
564 symbol size. The black rectangle represents the expected $\delta^{18}O$ and $\delta^{13}C$ values of marine
565 carbonate precipitated in equilibrium with Upper Cretaceous seawater (Steuber, 1999). B:
566 Cross-plot of $\delta^{18}O$ versus T(Δ47). Uncertainties are reported as 1SD of the mean out of
567 one to three replicates. Expected Upper Cretaceous seawater temperature range is
568 reported in the blue shaded area (Steuber, 1999).

569

570 Table 1. Stable isotope results ($\delta^{18}O$, $\delta^{13}C$ and Δ_{47}) of the samples set investigated.

Phase	n	$\delta^{18}O$		$\delta^{13}C$		Δ_{47}	$\Delta_{47\ errors}$ (‰)		T(Δ 47) error (1SD) (°C)			$\delta^{18}O$ water
		‰VPDB	±STD	‰VPDB	±STD	CDES90[1]	STD	SE	Mean[2]	Min	Max	‰SMOW[3]
Blocky cal.	3	**-10,77**	0,03	**0,56**	0,24	0,463	0,011	0,006	**81**	87	75	**0,8**
Blocky cal.	3	**-10,54**	0,08	**-0,91**	0,09	0,473	0,010	0,006	**76**	81	71	**0,4**
Matrix dol.	3	**-6,17**	0,14	**3,37**	0,13	0,515	0,016	0,009	**56**	63	50	**-1,6**
Matrix dol.	3	**-4,56**	0,04	**3,14**	0,1	0,500	0,004	0,002	**63**	65	61	**1,2**
Matrix dol.	3	**-6,32**	0,07	**3,39**	0,19	0,511	0,015	0,009	**58**	65	52	**-1,4**
Saddle dol.	1	**-10,59**		**0,17**		0,442			**92**	-	-	**-0,6**
Host rock	2	**-2,92**	0,05	**1,83**	0,04	0,624	0,043	0,030	**18**	32	6	**-1,9**
Host rock	2	**-2,94**	0,22	**1,82**	0,05	0,621	0,017	0,012	**19**	24	14	**-1,7**

"Note. Errors on average $\delta^{18}O$ and $\delta^{13}C$ are given as 1S.D. Errors on samples Δ_{47} and $T\Delta_{47}$ are 1 SD of the mean values calculated out of replicate Δ_{47} measurements of the same powder.
(n) is the number of replicate measurements of the same carbonate powder
[1] Δ_{47}CDES90 are values relative to the 'carbon dioxide equilibrium scale' CDES, without acid fractionation correction.
[2] Paleotemperatures calculated using the composite Δ_{47}-T calibration (Eq. 3 from Bonifacie et al. 2017)
[3] Oxygen isotope compositions of waters are calculated using $T\Delta_{47}$ and the equations of fractionation of oxygen isotopes between the carbonate and water of either O'Neil et al. (1969) for calcite and Horita (2014) for dolomite.

571

572 Multiple sulfur isotopes analysis on CAS resulted in $\delta^{34}S$ of 20.00‰ V-CDT ± 0.013‰, $\delta^{33}S$
573 of 10.28‰ V-CDT ± 0.016‰ and $\delta^{36}S$ of 37.85‰ V-CDT ± 0.091‰. From these values, $\Delta^{33}S$
574 and $\Delta^{36}S$ were calculated and yielded values of -0.487‰ ± 0.016‰ and -0.487‰ ±
575 0.091‰, respectively.

576 4.4 REE Patterns

577 REE concentrations were obtained from micritic limestones, matrix and saddle dolomites,
578 and the calcite cements. Figure 11 presents the PAAS-normalized REE patterns plotted on
579 a logarithmic scale. Micrites are more enriched in REE than the dolomite and calcite
580 phases. Also, the middle REE elements show a bulge pattern with slightly higher
581 concentrations than the light and heavy elements. In the case of the matrix dolomites, Tm
582 concentration was lower than the detection limit of the spectrometer and a valid
583 measurement was therefore not possible.

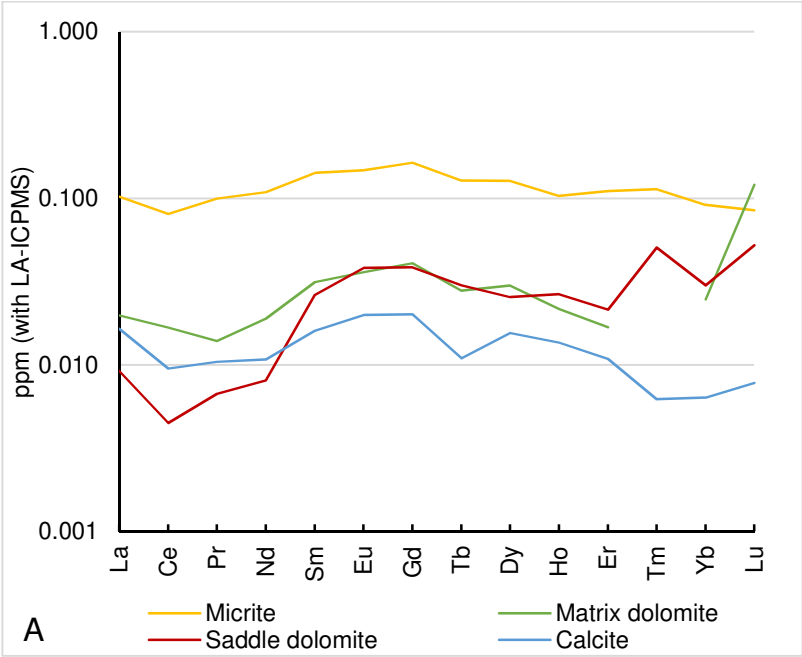

584

585 Figure 11. PAAS-normalized REE pattern of the micritic host rock, matrix dolomites,
586 saddle dolomite and calcite. Patterns of dolomite and calcite phases show a bulge (relative
587 enrichment) in the middle REE.

588 4.5 U-Pb LA-ICPMS absolute age dating

589 In order to obtain absolute dating with the U/Pb method on calcite and dolomite phases 15
590 measurements were performed with LA-ICPMS to estimate the U and Pb elemental
591 concentration. Obtained concentrations are in the range of 0.001 to 0.005 ppm for U and
592 Pb and were thus too low to meet the minimum requirement for absolute age dating.

593 4.6 Fluid inclusions thermodynamics modeling

594 Petroleum inclusion thermodynamic (PIT) and aqueous inclusion thermodynamic (AIT)
595 modeling were applied to the oil and aqueous inclusions of the blocky calcite. This step
596 allowed the construction of isochores for the two inclusion types and allowed to estimate
597 P-T conditions of trapping indicated by their intersection domain. The inclusions used are
598 coeval primary inclusions selected during petrographic analysis (part 4.2). The results
599 indicate a trapping temperature between 82 and 92°C at pressures of 136-210 bars
600 respectively. For the Albian reef located at a depth of 1400m, the double-isochore
601 technique was not possible due to the scarcity of aqueous inclusions and the difficulty in
602 accurately determining their co-genetic relationships with the oil FIs.

By using the confocal scanning microscopy and associated image processing, the volume of gas can be used to obtain a qualitative assessment of the type of trapped oil. Figure 12 displays the evolution of 8 different types of reference oils (Bourdet et al., 2008) with the results for Upper Lacq and Albian reef oils. The close association of the plotted Lacq oil to the North American Black Oil indicates that the Lacq oil is heavy.

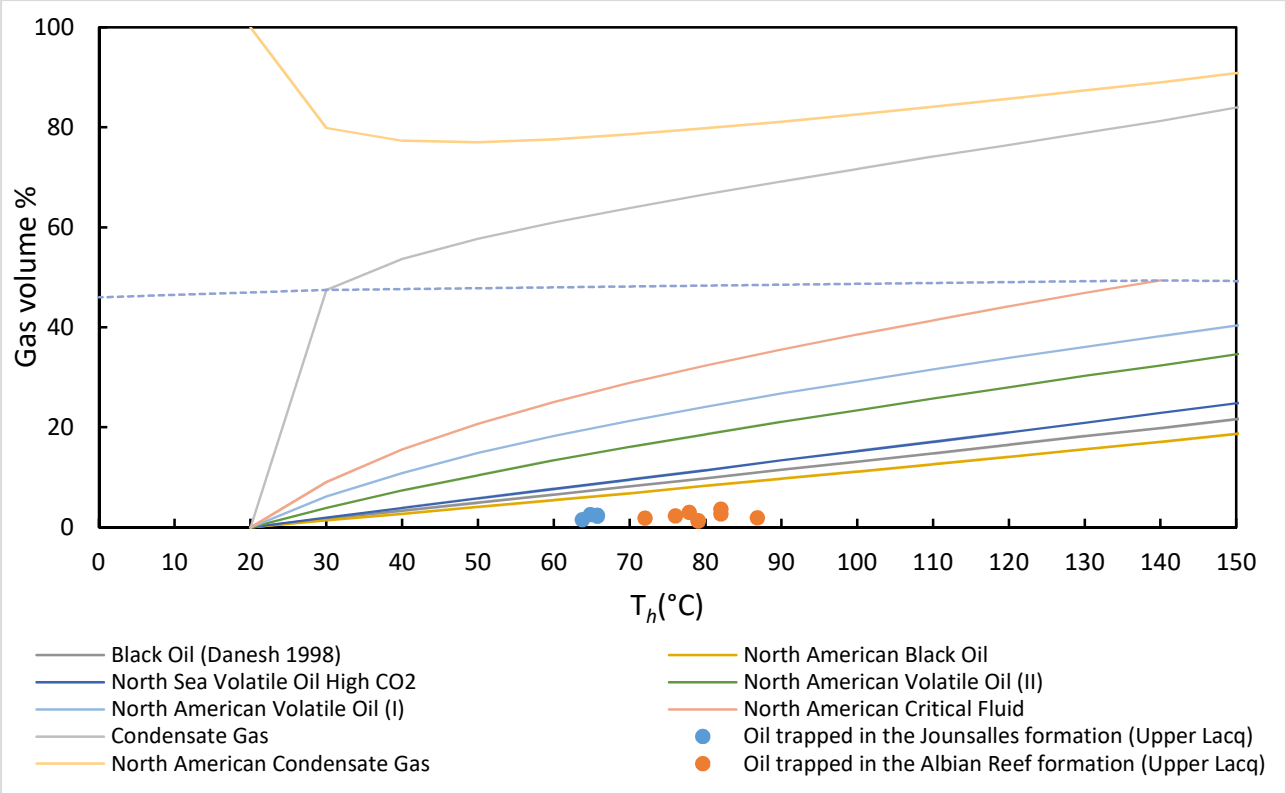

Figure 12. Gas volume % vs. T_h trends for 8 different reference oils with plotted results for Upper Lacq and Albian reef oils. L-V line separates the homogenization to the liquid domain below from the gas domain above. Modified after Bourdet et al., (2008).

4.7 Basin modeling

4.7.1 Basal heat flow scenario

Modeling the syn-rift to post-rift basal heat flow requires taking into account the thermal maturity of organic material using vitrinite reflectance data as well as the geodynamic history of Lacq since the late Aptian. This history includes (i) the Albo-Aptian rifting, followed by (ii) an erosion phase during the Late Albian - Early Cenomanian, (iii) a phase of post-rift cooling during the Cenomanian - end Santonian, and (iv) the principal inversion and shortening episode during the Eocene. These input data constrain a best-fit model

620 where the heat flow reaches a peak of about 130 mW/m^2 during the Aptian extension
621 before a decrease to nearly 56 mW/m^2 at the onset of N-S convergence. These values
622 were modeled to obtain an acceptable present-day geothermal gradient of 50°C/km. Such
623 a geothermal gradient is reasonable since the foreland basin was superimposed directly
624 on a still-hot rift with ongoing thermal subsidence that is driven by the post-rift thermal
625 cooling (Angrand et al., 2018).

626 4.7.2 Thermal history reconstruction constrained by vitrinite reflectance data

627 Vitrinite reflectance measurements are plotted according to their stratigraphic location in
628 figure 13. Basin modeling results in an acceptable fit between the modeled thermal
629 gradient (black line in figure 13) and the measured vitrinite reflectance values. The thermal
630 maturity of Upper Cretaceous formations follows a normal burial trend, interrupted by a
631 minor erosional event on the base Oligocene boundary. Our modeling assumes 200
632 meters of eroded material at the base Cenomanian unconformity, and 400 meters during
633 the maximum exposure at the base Oligocene unconformity. These values take into
634 account the shape of the onlaps and toplaps of reflectors on both sides of the
635 unconformities (Fig. 2).

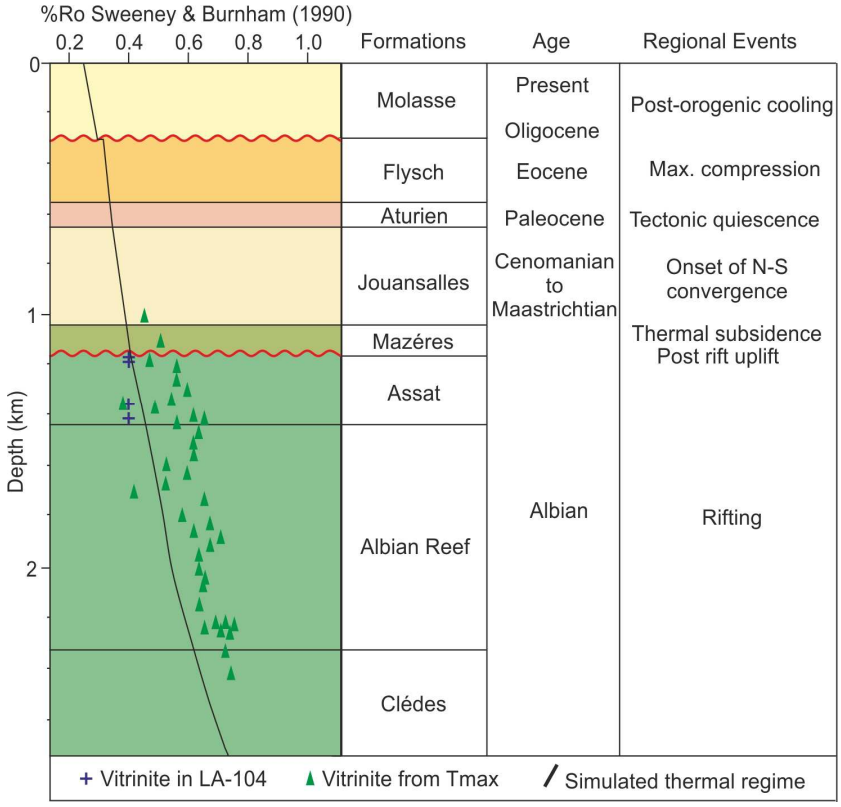

636

637 Figure 13. Simulated thermal regime in Petromod constrained by vitrinite reflectance
638 measurements.

639

640 # 5 Discussion

641 ## 5.1 Paragenesis and fluids involved

642 The chronological sequence of diagenetic phases deduced from petrographic observations

643 is represented in figure 14.

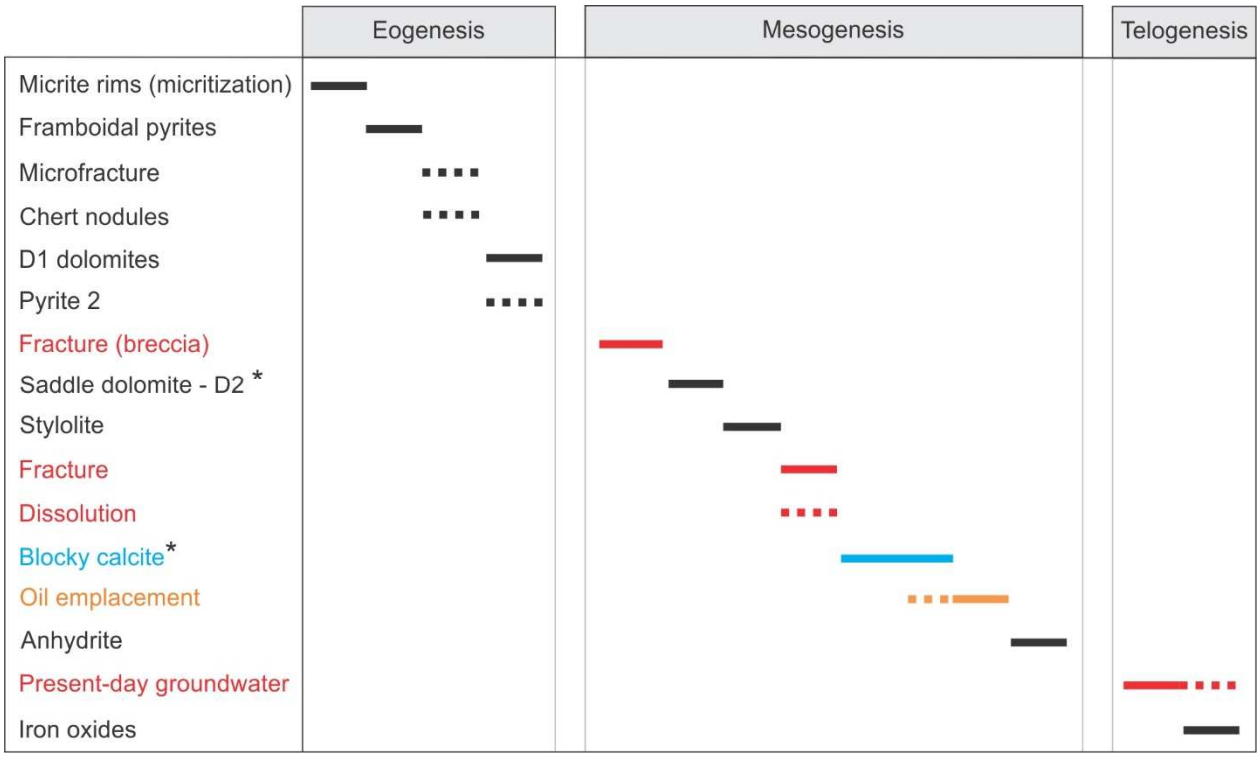

644

645 Figure 14. Chronology of diagenetic phases and fracturing events observed in Upper Lacq
646 from oldest at the top to youngest at the base. Dashed lines correspond to phases whose
647 exact paragenetic timing cannot be precisely constrained. Asterisks* indicate the phases
648 investigated here in thermometric studies (FI and Δ_{47}).

649 The wackestone/packstone facies precipitating in a shallow marine depositional
650 environment has been characterized by Δ_{47} thermometry. Carbonate clumped isotopes
651 show surface temperatures around 20°C and $\delta^{18}O$ of parent fluids around -1.9 ‰SMOW
652 (Table 1). These values (1) point towards precipitation conditions in a shallow marine
653 depositional environment, by marine fluids with a potential meteoric water influx and (2)
654 demonstrate the absence of significant recrystallization of the host-rock during burial.

655 During eogenesis, microborers and bacterial activity resulted in destructive micritization of
656 carbonate clasts with the micrite envelope developing from the edges to the center of the
657 grain (Bathurst, 2007). Framboidal pyrites precipitated as a result of bacterial sulphate
658 reduction (BSR) of organic matter just below the surface of the sediment (Machel, 2001).
659 Such an interpretation is supported by the distribution of framboidal pyrites that are mainly
660 associated with skeletal grains and micritized rims. The relative timing of silicification is
661 difficult to constrain as chert nodules were observed only in micritic, non-dolomitized
662 samples. However, given the occurrence of siliceous sponges (Fig. 4f), the timing was

663 relatively early as diagenesis of amorphous organic silica is favored by pH variations due
664 to the degradation of organic matter at low temperature during early burial (Hinman, 1990).
665 Silica was provided by siliceous sponges after the death of organisms and locally
666 reprecipitated by replacement of the micritic matrix. Early diagenesis ends with the D1
667 dolomites. Their non-luminescence and $\delta^{18}O$ of parent fluids of -1.6 to +1.2‰SMOW
668 (Table 1) suggest a mixing between oxidizing meteoric fluids and trapped formation fluids,
669 of a marine origin, that can provide Mg needed for this volumetrically-limited dolomite
670 phase. Since the bulk powders extracted from the matrix dolomites are a mixture of D1
671 and D2 dolomite phases, the Δ_{47} temperature of around 60°C could reflect an average
672 between these two end-members. Pyrite 2 post-dates D1 rhombs since relics of D1 were
673 observed inside pyrites. Merino and Canals (2011) argue that if the dolomitizing fluids
674 contain some metals, and if enough organic matter is present in the host carbonates,
675 pyrites should precipitate during and after the dolomitization phase by the reduction of
676 aqueous sulphates released from organic carbon. The non-ferroan composition of all
677 dolomite phases in Upper Lacq, as well as contacts between some pyrite 2 and the D1
678 dolomite are in accordance with such a mechanism. Any Fe^{2+} in the dolomitizing fluids was
679 likely consumed by the precipitation of reduced sulfur species, and the dolomitizing fluid
680 was then depleted in iron. The scarce distribution and limited quantity of pyrites observed
681 suggest that initially the quantity of Fe^{2+} in the dolomitizing fluids was actually low. A
682 similar mechanism has been demonstrated in the Neogene Monterey and Sisquoc
683 Formations in Santa Maria Basin, California (Compton, 1988).

684 During mesogenesis, the Upper Lacq reservoir experienced its main diagenetic
685 modifications. Here we consider that mesogenesis is the burial domain isolated from
686 surface-related processes while telogenesis occurs only the late stage of exhumation
687 when oxidizing surficial fluid enter in the diagenetic system. Mesogenesis started with an
688 episode of fracturing and brecciation that generated new pathways for dolomitizing fluids.
689 Some breccias are cross-cut and cemented by D2 and saddle dolomite, suggesting that

690 these dolomites formed during or just after fracture opening. Therefore, after the early D1
691 phase, new dolomitizing fluids circulated along fractures and precipitated D2 as
692 overgrowth cements in intercrystalline pores or as pore-filling saddle dolomite crystals in
693 the open fractures. This dolomitization possibly occurred under high pressures given the
694 occurrence of breccia and fractures in these dolomitized facies. Differences in dolomite
695 sizes and extinction behavior can be attributed to the crystallization space available
696 (Machel, 2004). Using Δ_{47} temperatures, more depleted values of -0.6 ‰SMOW were
697 obtained for D2. These isotopic signatures point toward a marine source different than the
698 meteoric parent fluids of D1.

699 Post-dolomitization diagenesis involved fracturing, calcite cementation, and oil migration. A
700 second fracturing phase preceded the precipitation of the blocky calcite. FIs in calcite have
701 a T_h range of 70-90°C with highest modes at 80°C, with salinities being equal to or lower
702 than that of seawater (Fig. 9b). The $\delta^{18}O$ of the parent-fluids precipitating the calcite is in
703 the range of +0.4 to +0.8‰SMOW (table 1), typical of a marine source. The opening of
704 new fractures and circulation pathways for the parent-fluids of the blocky calcite may have
705 connected the Upper Lacq reservoir with new reservoirs of trapped connate fluids depleted
706 in Mg. This fluid pulse is distinct from that responsible for dolomite precipitation especially
707 in that it is associated with oil migration.

708 Several pulses of oil migration can explain the coexistence of two types of oil inclusions in
709 the same calcite cement. Scarce inclusions with a strong white fluorescence, and
710 containing water, as indicated by FT-IR spectra, are probably more mature than inclusions
711 with brown fluorescence. They are therefore associated with a second pulse of oil
712 migration. A third pulse is assumed to be responsible for the oil coatings on top of calcite.
713 This last pulse was important enough to allow an economically valuable infill of the Upper
714 Lacq reservoir. PIT modeling also demonstrates that the oil trapped as inclusions in the
715 blocky calcite phase is heavy. This is in agreement with Connan and Lacrampe-Couloume

716 (1993) who propose that the oil in Upper Lacq originally migrated as heavy oil and was not
717 a consequence of post-migration modifications.

718 After calcite cementation and oil emplacement, anhydrites precipitated. The multiple sulfur
719 isotopes signatures of CAS are listed in Table 2 and are compared with the Eocene
720 marine fluids signatures (Crockford et al., 2019 and references therein). The overlap in the
721 results indicates a marine seawater origin for the parent fluids.

722 Table 2. Multiple sulfur isotope signature of CAS from anhydrite-rich samples (this study)
723 and those of the reference Eocene seawater of Crockford et al. (2019) and references
724 therein.

	This study		Eocene marine water	
	Value (‰ V-CDT)	Error (‰ V-CDT)	Value (‰ V-CDT)	Error (‰ V-CDT)
$\delta^{34}S$	20.00	± 0.013	22.87	± 7.86
$\Delta^{33}S$	0.036‰	± 0.016	-0.001	± 0.042
$\Delta^{36}S$	-0.487‰	± 0.091	0.713	± 0.508

725

726 The relative enrichment of seawater with calcium sulphates provided a source for this
727 anhydrite phase, which can precipitate after Mg depletion, as previously documented in
728 the dolomitized Devonian reservoirs of Alberta, Canada (Butler, 1970; Mountjoy et al.,
729 1999; Machel, 2004).

730 During telogenesis, meteoric fluids were laterally re-introduced in the diagenetic system.
731 Vertical input is unlikely given the integrity of the Paleocene seal. Late input of meteoric
732 fluids is supported by the occurrence of present-day groundwater in the Upper Lacq
733 reservoir at a depth of -723 m. Groundwater samples, collected from Upper Lacq, were
734 analyzed for their δD and $\delta^{18}O$ isotopes by Esquevin et al. (1987) and are plotted against
735 the Global Meteoric Water Line (GMWL) in figure 15. The results show that the
736 groundwater in Upper Lacq is slightly modified and enriched with $\delta^{18}O$ relative to the
737 GMWL. This minor enrichment could be the result of fluid-rock interactions and possible
738 contributions of $\delta^{18}O$-enriched formation fluids. This minor enrichment could result from
739 the mixing of $\delta^{18}O$-enriched pore fluids with more recent meteoric water recharges.

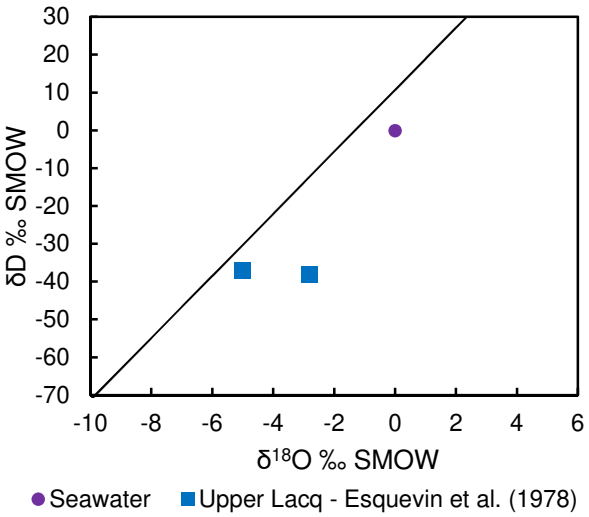

740

741 Figure 15. δD vs. $\delta^{18}O$ in ‰ SMOW for the groundwater collected from Upper Lacq plotted
742 against the Global Meteoric Water Line (GMWL). The slight enrichment compared to the
743 GMWL could be the result of mixing with $\delta^{18}O$ – enriched formation fluids or contamination
744 by the host rock.

745 The mixing of this groundwater with H_2S, currently present in and commercially extracted
746 from the Lacq reservoirs may contribute to sulfuric acid speleogenesis (SAS) that can
747 explain the karstic cavity at a depth of nearly 2200 m reported in the drilling reports of LA –
748 101. Similar cases of SAS have been recently documented in Jurassic and Cretaceous
749 carbonates of the north Pyrenean foothills and the southern Aquitaine foreland basin
750 (Laurent et al., 2019).

751 In summary, three different origins of fluids contributing to diagenesis can be documented;
752 these are: (1) a mixture of meteoric and marine fluids precipitating D1 dolomites, (2)
753 another mixture of marine and clay-released fluids for saddle dolomite, calcite and
754 anhydrite cements, and then a (3) modified meteoric source for the present day
755 groundwater in the reservoir.

756 An important criterion to consider here is the amount of magnesium required for
757 dolomitization and its possible sources. Several sources can been involved such as: (a)
758 Mg derived from the Triassic evaporites of the core of the Lacq anticline, (b) serpentization
759 reactions close to the exhumed mantle domain, which could have released Mg into the
760 fluids, (c) Mg-rich fluids released from the compaction and dewatering processes of the
761 Albo-Aptian Ste-Suzanne and Assat marls. Mg sourced from the salt diapir in the core of

762 the anticline is ruled out because of the very low salinities measured in the aqueous fluids
763 inclusions of the D2 and saddle dolomite phases.

764 Serpentization- or mantle-derived Mg from the exhumed mantle domain is plausible given
765 the geodynamic setting and the proximity to the exhumed mantle bodies, e.g. Sarrance
766 anticline and Arbailles Massifs (Salardon et al., 2017). However, such a deep source
767 would provide higher values of $\delta^{18}O‰$ SMOW and inclusions should contain evidence of
768 mantle-derived CO_2 or H_2. The lack of supporting evidence in the studied samples makes
769 it difficult to support this hypothesis.

770 Clay dewatering is a very likely candidate to provide the amount of Mg required for
771 dolomitization. The Apto-Albian Sainte Suzanne and Assat Marl formations reach
772 considerable thicknesses of more than 5 km in the southern Lacq basin (Fig. 2; Biteau et
773 al., 2006). Such a thickness would contain enough Mg, trapped in formational fluids that
774 were expelled along faults and fractures and dolomitized the Upper Lacq reservoirs.
775 Fluids generated by dewatering are characterized by low salinities because of the
776 reduction of the total dissolved salts (TDS) through clay ultrafiltration (Tremosa et al.,
777 2019), an increase in the $\delta^{18}O$ signature upon clay dehydration (Minami et al., 2018), and
778 an enrichment in Mg due to the diagenetic smectite-illite transformations (Schrijver et al.,
779 1996).

780 As supported by the isotope geochemistry, the parent fluids of saddle dolomites and
781 calcites were marine in origin. These marine fluids, trapped as connate waters in deep part
782 of the basin, were expulsed during the first fracturing phase that opened new circulation
783 pathways. During their migration they were modified by mixing with low salinity Mg-rich
784 fluids generated by clay dewatering.

785 5.2 Redox conditions

786 The nonluminescence of D1 dolomites and the contribution of meteoric fluids, at very
787 shallow depths suggest that the first dolomitizing fluids were oxidizing. Later fluids involved

788 in saddle dolomitization and calcite cementation were relatively enriched in middle REE
789 (MREE). Such a REE pattern can be interpreted as the signature of fluids circulating in a
790 reducing environment (Haley et al., 2004). Further indications of this reducing state are
791 provided by the dull red and dull orange luminescence of the saddle dolomite and calcite
792 respectively (Barnaby and Rimstidt, 1989). In addition, such a reducing system is also in
793 agreement with the presence of not biodegraded and unoxidized oil inclusions in calcites.
794 During telogenesis, oxidizing conditions were recovered with the present-day groundwater
795 (Figs. 14 and 15) at the origin of the oxidization of the pyrite 2.

796 5.3 Hydrothermal activity

797 To better constrain the evolution of P-T conditions during the burial history of the Upper
798 Lacq reservoir, fluid pressure gradients need to be estimated. Figure 16 illustrates the
799 evolution of hydrostatic and lithostatic pressure gradients experienced by the Upper Lacq
800 reservoirs assuming a geothermal gradient decreasing from 110°C/km during the peak
801 Aptian rifting to 50°C/km in the present day (Angrand et al., 2018; Renard et al., 2019).
802 Cooling between 88.6 and 83.5 Ma is a continuation of the isostatic rebound after the
803 Aptian rifting. The loop in the gradients (between 40 and 33.9 Ma) is the caused by the
804 base Oligocene unconformity. The grey shaded area named (A) represents the range of
805 trapped P-T conditions obtained with PIT-AIT modeling. These conditions are not in
806 equilibrium with the thermal evolution of the reservoir. The good match observed between
807 temperature estimates based on two independent geothermometers (fluid inclusions with
808 the double isochore technique and carbonate clumped isotope thermometry, figure 16)
809 strongly support the reliability and accuracy of each thermometer (c.f. see Mangenot et al.,
810 2017). The two techniques reveal a thermal disequilibrium between the mineralizing fluid
811 and the host-rock. Indeed, a gap of at least 30-40°C, between the maximum burial
812 temperatures and the minimum trapping conditions, is observed. This suggests that the
813 parent fluids of calcites and similarly of dolomites were hotter than the burial temperatures
814 and hence imply the involvement of hot hydrothermal fluids.

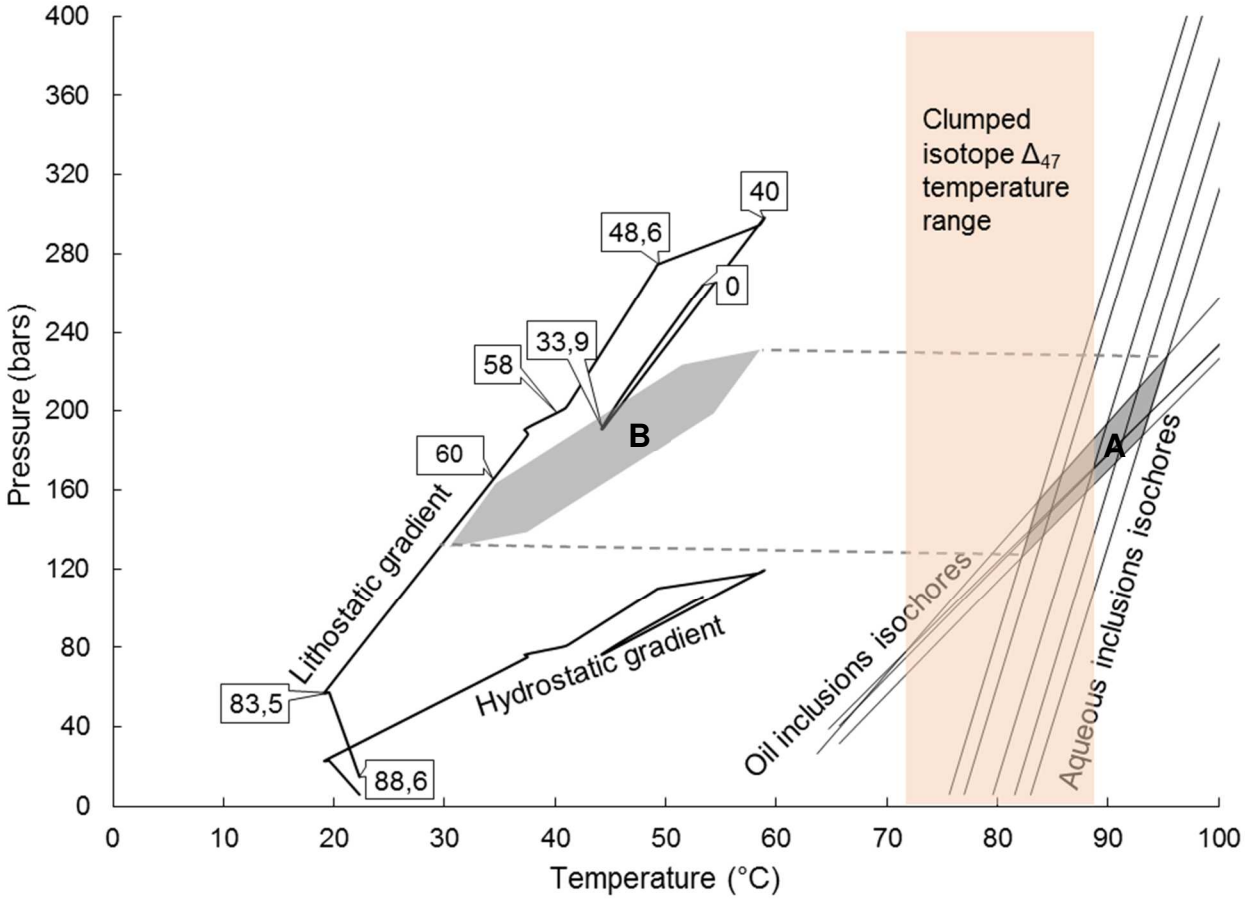

Figure 16. P-T trapping conditions and evolution of fluid pressure gradients simulated with Petromod-1D and PIT-AIT respectively. Numbers in tags are ages in Ma. The pink area represents the calcite temperature estimation deduced from Δ_{47} thermometry (i.e. an isotopic thermometer independent of any pressure effect). The grey shaded area (A) is the intersection of both isochore types and hence indicates the trapping conditions of inclusions in blocky calcites. The loop in the hydrostatic and lithostatic gradients represent the base Oligocene unconformity at 40-34 Ma. The dashed lines correspond to the extrapolation of the P-T conditions in (A) to the shaded area (B) in the domain between the hydrostatic and lithostatic fluid pressure.

However, by extrapolating the pressure range of the fluids to the domain between hydrostatic and lithostatic gradients (dashed lines in figure 16), a timing between 60 and 40 Ma can be estimated from the shaded area (B). This age corresponds to the Selandian-Bartonian (Paleocene to mid-Eocene), during the Pyrenean compression. In the Rousse reservoir, 30 km southeast of Lacq (Fig. 1), Renard et al. (2019) concluded that one of the two fluid pulses experienced by the Rousse system was due to Eocene Pyrenean tectonic compression. By measuring the difference between the trapped FI pressure and the hydrostatic pressure gradient, an overpressure of nearly 80 bars can be estimated. Such an overpressure is very common in oil-producing anticlines.

Further evidence that supports the hydrothermal activity are data provided by the well LA-415 (400m east of LA-37, Figs. 1 and 2). This horizontal NNE-SSW-oriented well on the crest of the Lacq anticline penetrated the productive reservoirs of Upper Lacq and cross-cut N100° and N60° trending vertical fractures (Fig. 17). The close association of fractures and dolomite bodies was interpreted as evidence of fracture-controlled hydrothermal dolomitization (Lambert et al., 2006).

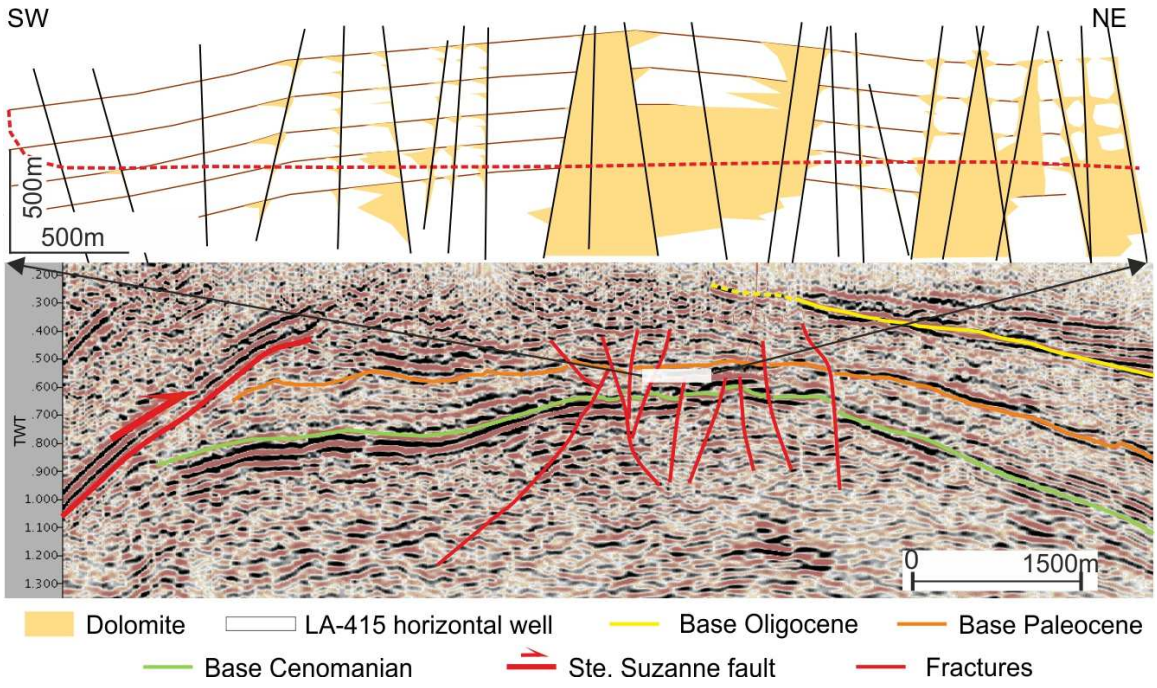

Figure 17. Schematic model of the distribution of dolomite bodies and fractures in the Upper Lacq reservoir based on observations in the well LA-415 (red dashed line). The fractures drawn in the scheme are located on the larger scale NE-SW seismic cross section (Based on Lambert et al., 2006).

5.4 Fluid circulation schemes

A synthesis diagram of all fluids involved in the diagenetic evolution of the Upper Cretaceous Upper Lacq reservoir, their circulation pathways and resulting products are summarized in figure 18. The early oxidizing meteoric fluids involved in the precipitation of the D1 dolomite rhombs are relatively early since the Paleocene seal was not in place to prevent the vertical circulation of fluids to the reservoir. Reflux and mixing zone (or dorag) dolomitization models can explain this process in a lagoonal and shallow marine setting on the carbonate platform behind the Albian reef barrier. The evaporated seawater percolating downwards and the interstitial formation fluids provided the Mg required for this

854 minor dolomitization phase. When the Paleocene flysch was deposited, the vertical supply
855 of meteoric fluids was interrupted. The clay-released fluids from the thick Albo-Aptian
856 formations in the Southern Lacq basin (Fig. 2) became the dominant fluids involved in
857 hydrothermal dolomitization (Fig. 18). The Sainte Suzanne Fault, activated during the
858 Eocene compression, could have provided a pathway for the circulation of deep connate
859 hot fluids from the Southern Lacq Basin to the relatively cooler, lower pressure area on the
860 crest of the Lacq anticline. This fault crosscuts the clay-rich Albo-Aptian formations (i.e.
861 Sainte Suzanne and Assat marls), which, upon fracturing and squeezing, may have
862 released Mg-rich fluids with low salinity. Additional Mg could have been provided by the
863 precursor D1 dolomites, which were partially dissolved upon fracturing and brecciation.

864 The early reflux to mixing zone dolomitization model agrees with previous interpretations
865 that considered the dolomites of Upper Lacq as being early products that precipitated in a
866 shallow marine evaporitic platform (Bouroullec et al., 1986; Le Marrec et al., 1995).
867 However, the overpressured hydrothermal activity that formed the bulk of the dolomite
868 bodies of Upper Lacq was not previously considered.

869

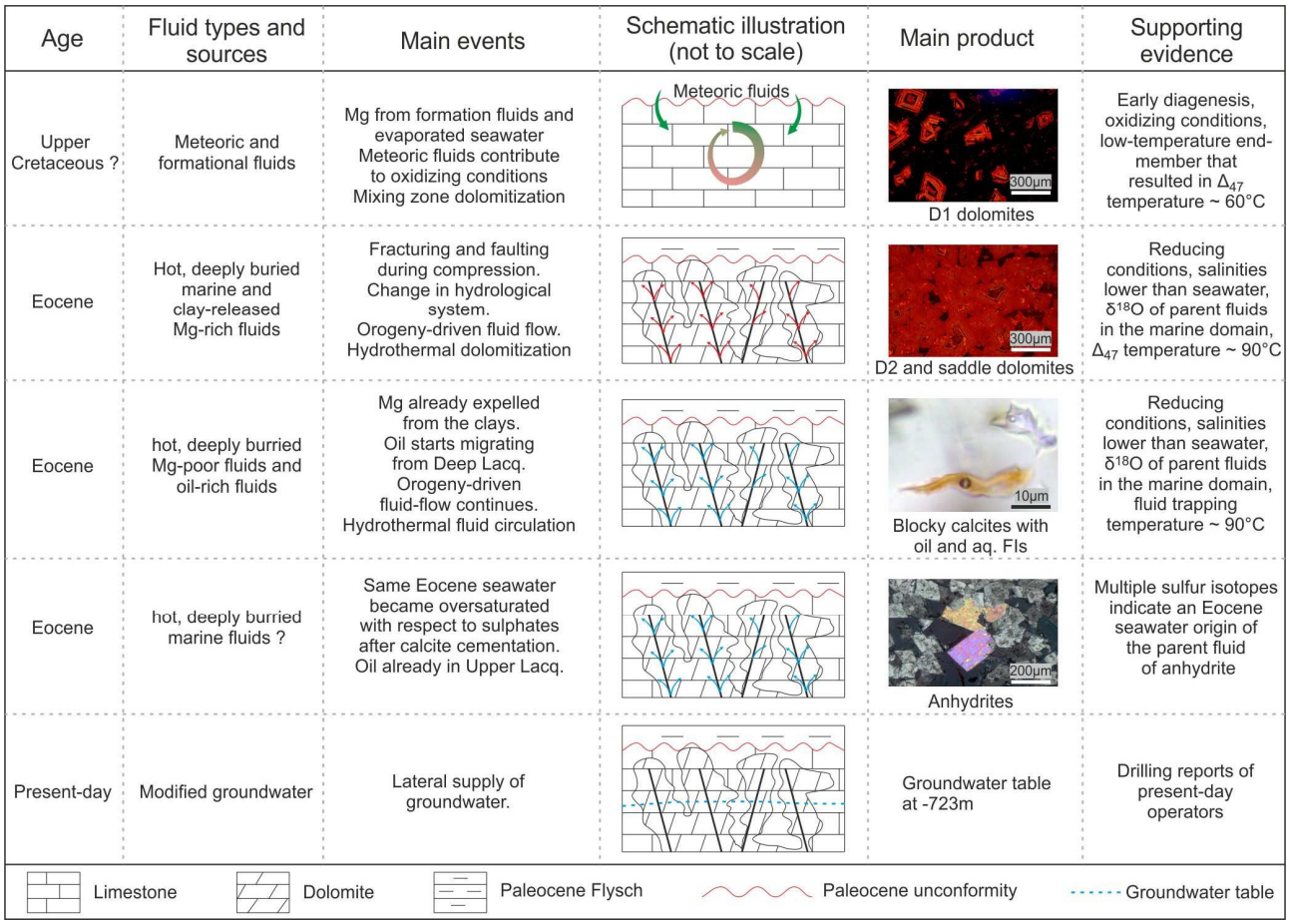

Figure 18. Summary diagram of fluid circulation schemes with their main products.

Stress variations in and around a seismically active fault system would affect local fluid pressures and allow the mobilization of considerable volumes of fluids (Sibson et al., 1975). This orogeny-driven style of fluid migration was involved in the dolomitization of the Albian carbonates of the Asón valley in the Basque Cantabrian Basin of northern Spain (López-Horgue et al., 2010), the middle Jurassic oil reservoirs of the Paris Basin (e.g. Carpentier et al., 2014; Mangenot et al., 2018b) and the dolomitized carbonates in the St. George Group of western Newfoundland, Canada (Conliffe et al., 2010). The new fracturing event that preceded calcite cementation probably connected the Upper Lacq reservoir with another reservoir of fluids. This is supported by the fact that the new fluids are depleted with respect to dolomite and the associated oil migration started only with calcite cementation. The new fracturing stage was probably linked to modifications in regional tectonic stress that have affected the intensity of clay dewatering and

885 consequently the amount of Mg expelled. Fluid and basin modeling suggest that also
886 during the Eocene compression, these circulating fluids were not in thermal equilibrium
887 with the host rocks (Fig. 16). These Ca-rich fluids have possibly mixed with oil-rich fluids
888 expulsed from the Deep Lacq source rocks as new fluid pathways opened and the
889 connection with new fluid reservoirs started during this second fracturing stage. The origin
890 of oil in Upper Lacq is debated given complexities in the structural and thermal evolution of
891 the petroleum system (Connan and Lacrampe-Couloume, 1993; Le Marrec et al., 1995;
892 Serjoune, 1995; Houzay et al., 2008). However, the most probable scenario is a
893 dysmigration from the Deep Lacq source rocks passing through the Albian reefs. This
894 circulation scheme was documented by the correlation of sterane distribution patterns
895 between the Deep Lacq source rocks, Albian reefs and oils of the Upper Lacq reservoir.
896 Connan and Lacrampe (1993) concluded that oils found in Upper Lacq migrated from the
897 Jurassic-Barremian sources rocks laterally through the reef to accumulate in Upper Lacq.
898 The abundance in oil inclusions observed in the Albian reef samples is also in agreement
899 with this scenario of oil migration. Therefore, lateral flow of connate (marine) fluids mixed
900 with the migrating oil and precipitated blocky calcites rich in oil and aqueous inclusions.

901 Multiple sulfur isotopes indicate an Eocene marine origin for the parent fluids of anhydrites.
902 Thermodynamically, the solubility of calcite is reduced in sulphate rich solutions and
903 $CaCO_3$ would be the first mineral that precipitates (Li and Duan, 2011). Since the timing of
904 calcite cementation is also mid-Eocene in age, we suggest that the marine parent-fluid of
905 anhydrite was the same as the parent-fluid of calcites. Because of the precipitation of
906 blocky calcite, the fluid became gradually depleted in CO_3^{2-} and permitted the precipitation
907 of anhydrite (Fig. 18). The precipitation of this sulphate phase is typical for solutions
908 originating from marine to modified marine fluids as documented in the Devonian
909 reservoirs of Alberta, Canada (Butler, 1970; Mountjoy et al., 1999; Machel, 2004).

910 Finally, during uplift and telogenesis, differences in hydraulic heads from nearby elevated
911 areas would provide a suitable driving mechanism for the lateral supply of the crest of the
912 anticline with the present-day groundwater (Fig. 18).

913 6 Conclusion

914 A revised paragenesis for the Upper Cretaceous Upper Lacq oil reservoir is presented
915 where the evolution of the Pyrenean domain and the Aquitaine foreland basin have played
916 a major role in controlling the timing of carbonate reservoir diagenesis. We argue that at
917 least three fluid sources where involved in the diagenetic modifications of the Upper Lacq
918 reservoir.

919 After shallow-marine carbonate deposition and early bacterial diagenesis during the Late
920 Cretaceous, a mixture of marine fluids during reflux evaporation in a lagoonal setting,
921 together with formational fluids allowed the precipitation of the early D1 dolomite phase.
922 Microthermometric and chemical evidence support a model with multiple fluid pulses
923 driven by regional orogenic forces. After the deposition of the Paleocene seal and during
924 the Major orogenic compressive phase, Mg-rich, low salinity, hot, relatively deep fluids
925 from the Southern Lacq Basin migrated along the Saint Suzanne and Lagor thrust faults,
926 under a state of thermal disequilibrium being at least 30-40°C hotter than the ambient host
927 rocks. These fluids dolomitized the Upper Lacq reservoir. After the end of Mg expulsion
928 from Albian clays of the Southern Lacq Basin, due to modifications in regional tectonic
929 stress, hot low-saline fluids continued to be squeezed out of this basin and towards Upper
930 Lacq. The combination of the Mg-poor, hot, low salinity fluid from the Southern Lacq Basin
931 and the oil that migrated from the Deep Lacq source rocks precipitated blocky calcites rich
932 in oil and aqueous inclusions. AIT-PIT and basin modeling also suggest an Eocene timing
933 for this fluid pulse. After calcite cementation, the remaining fluids became oversaturated
934 with respect to sulphates and a minor phase of anhydrite precipitated. The timing of
935 anhydrite precipitation is supported by the multiple sulfur isotopes that indicate an Eocene
936 seawater signature of the parent fluid. Finally, during telogenesis, oxidizing fluids were

reintroduced possibly by lateral input because the overlying Paleocene flysch seal would inhibit downward percolation of fluids.

In conclusion, by using a multidisciplinary petrographic, geochemical and modeling approach we provide evidence that the main diagenetic events in the southern Aquitaine basin were mainly linked to the Pyrenean convergence during the Eocene. Even if a minor early dolomitization event cannot be totally ruled out, orogeny-driven hydrothermal dolomitization is the principal mechanism that affected the Upper Cretaceous carbonate reservoirs in the Lacq area.

7 Acknowledgments

This work was funded by the *Centre de Recherches sur la Géologie des Matières Premières Minérales et Energétiques* (CREGU), contract number FR00008500-FR00009038, and TOTAL EP-R&D. Sylvain Calassou and the colleagues from the *Centre Scientifique et Technique Jean Féger* de *TOTAL* (CSTJF-TOTAL) are warmly thanked for providing access to their facilities and data archives to conduct this research. The authors are grateful to the constructive comments and revisions of Enrique Gomez-Rivas and an anonymous reviewer that have greatly improved the quality of the manuscript. Olivier Fonta from GEOPETROL is thanked for giving access and permission to acquire core samples. Laurine Duvivier is acknowledged for her input on the basin modeling. Pierre Cartigny from the Institut de Physique du Globe de Paris (IPGP) is kindly acknowledged for his assistance with the multiple sulfur isotopes analysis. John Eiler and Nami E. Kitchen from California Institute of Technology (Caltech) are warmly thanked for their help and support with the clumped isotope analysis.

959 8 References

960 Angrand, P., Ford, M., Watts, A.B., 2018. Lateral Variations in Foreland Flexure of a Rifted
961 Continental Margin: The Aquitaine Basin (SW France). Tectonics 37, 430–449.
962 https://doi.org/10.1002/2017TC004670

963 Barnaby, R.J., Rimstidt, J.D., 1989. Redox conditions of calcite cementation interpreted
964 from Mn and Fe contents of authigenic calcites. Geol. Soc. Am. Bull. 101, 795–804.
965 https://doi.org/10.1130/0016-7606(1989)101<0795:RCOCCI>2.3.CO;2

966 Bathurst, R.G.C., 2007. Boring algae, micrite envelopes and lithification of molluscan
967 biosparites. Geol. J. 5, 15–32. https://doi.org/10.1002/gj.3350050104

968 Beaudoin, N., Bellahsen, N., Lacombe, O., Emmanuel, L., 2011. Fracture-controlled
969 paleohydrogeology in a basement-cored, fault-related fold: Sheep Mountain Anticline,
970 Wyoming, United States. Geochemistry, Geophys. Geosystems 12, n/a-n/a.
971 https://doi.org/10.1029/2010GC003494

972 Bilotte, M., Odin, G.S., Vrielynck, B., 2001. Geology and Late Cretaceous
973 palaeogeography of the geological site at Tercis les Bains (Landes , France), in: Odin,
974 G.S. (Ed.), The Campnanian - Maastrichtian Boundary. Elsevier Science B.V.

975 Biteau, J., Le Marrec, A., Le Vot, M., Masset, J.-M., 2006. The Aquitaine Basin. Pet.
976 Geosci. 12, 247–273. https://doi.org/10.1144/1354-079305-674

977 Boni, M., Parente, G., Bechstädt, T., De Vivo, B., Iannace, A., 2000. Hydrothermal
978 dolomites in SW Sardinia (Italy): evidence for a widespread late-Variscan fluid flow
979 event. Sediment. Geol. 131, 181–200. https://doi.org/10.1016/S0037-0738(99)00131-
980 1

981 Bonifacie, M., Calmels, D., Eiler, J.M., Horita, J., Chaduteau, C., Vasconcelos, C., Agrinier,
982 P., Katz, A., Passey, B.H., Ferry, J.M., Bourrand, J.-J., 2017. Calibration of the
983 dolomite clumped isotope thermometer from 25 to 350°C, and implications for a

984 universal calibration for all (Ca, Mg, Fe)CO3 carbonates. Geochim. Cosmochim. Acta
985 200, 255–279. https://doi.org/10.1016/j.gca.2016.11.028

986 Bourdet, J., Pironon, J., Levresse, G., Tritlla, J., 2008. Petroleum type determination
987 through homogenization temperature and vapour volume fraction measurements in
988 fluid inclusions. Geofluids 8, 46–59. https://doi.org/10.1111/j.1468-8123.2007.00204.x

989 Bouroullec, J., Leduc, J.P., Chennaux, G., Sanz, M.C., 1986. Etude lithfaciologique de 2
990 series de Lacq Superieur, LA.80 et LA.408, TOTAL EP internal report.

991 Brand, W.A., Assonov, S.S., Coplen, T.B., 2010. Correction for the 17O interference in
992 δ(13C) measurements when analyzing CO2 with stable isotope mass spectrometry.
993 Pure Appl. Chem. 82, 1719–1733. https://doi.org/10.1351/PAC-REP-09-01-05

994 Butler, G., 1970. Holocene gypsum and anhydrite of the Abu Dhabi sabkha, Trucial Coast:
995 an alternative explanation of origin, in: Rau, J., Dwelling, L. (Eds.), Third Symposium
996 on Salt. Northern Ohio Geological Society, Cleaveland, pp. 120–152.

997 Canerot, J., 1991. Comparative study of the Eastern Iberides (Spain) and the Western
998 Pyrenees (France) Mesozoic basins. Palaeogeogr. Palaeoclimatol. Palaeoecol. 87, 1–
999 28. https://doi.org/10.1016/0031-0182(91)90128-E

1000 Carpentier, C., Brigaud, B., Blaise, T., Vincent, B., Durlet, C., Boulvais, P., Pagel, M.,
1001 Hibsch, C., Yven, B., Lach, P., Cathelineau, M., Boiron, M., Landrein, P., Buschaert,
1002 S., 2014. Impact of basin burial and exhumation on Jurassic carbonates diagenesis
1003 on both sides of a thick clay barrier (Paris Basin, NE France). Mar. Pet. Geol. 53, 44–
1004 70. https://doi.org/10.1016/j.marpetgeo.2014.01.011

1005 Caumon, M.C., Tarantola, A., Mosser-Ruck, R., 2015. Raman spectra of water in fluid
1006 inclusions: I. Effect of host mineral birefringence on salinity measurement. J. Raman
1007 Spectrosc. 46, 969–976. https://doi.org/10.1002/jrs.4708

1008 Choquette, P.W., Pray, L.., 1970. Geologic nomenclature and classification of porosity in

1009 sedimentary carbonates. Am. Assoc. Pet. Geol. Bull. 54, 207–250.

1010 Clerc, C., Lagabrielle, Y., 2014. Thermal control on the modes of crustal thinning leading
1011 to mantle exhumation: Insights from the Cretaceous Pyrenean hot paleomargins.
1012 Tectonics 33, 1340–1359. https://doi.org/10.1002/2013TC003471

1013 Clerc, C., Lahfid, A., Monié, P., Lagabrielle, Y., Chopin, C., Poujol, M., Boulvais, P.,
1014 Ringenbach, J.-C., Masini, E., de St Blanquat, M., 2015. High-temperature
1015 metamorphism during extreme thinning of the continental crust: a reappraisal of the
1016 North Pyrenean passive paleomargin. Solid Earth 6, 643–668.
1017 https://doi.org/10.5194/se-6-643-2015

1018 Compton, J., 1988. Sediment Composition and Precipitation of Dolomite and Pyrite in the
1019 Neogene Monterey and Sisquoc Formations Santa Maria Basin Area California.
1020 SEPM Spec. Publ. 43.

1021 Conliffe, J., Azmy, K., Gleeson, S.A., Lavoie, D., 2010. Fluids associated with
1022 hydrothermal dolomitization in St. George Group, western Newfoundland, Canada.
1023 Geofluids 10, 422–437. https://doi.org/10.1111/j.1468-8123.2010.00295.x

1024 Connan, J., Lacrampe-Couloume, G., 1993. The Origin of the Lacq Superieur Heavy Oil
1025 Accumulation and of the Giant Lacq Inferieur Gas Field (Aquitaine Basin, SW France),
1026 in: Bordenave, M.L. (Ed.), Applied Petroleum Geochemistry. Editions Technip, Paris,
1027 pp. 464–488.

1028 Corre, B., Boulvais, P., Boiron, M.C., Lagabrielle, Y., Marasi, L., Clerc, C., 2018. Fluid
1029 circulations in response to mantle exhumation at the passive margin setting in the
1030 north Pyrenean zone, France. Mineral. Petrol. 0, 1–24.
1031 https://doi.org/10.1007/s00710-018-0559-x

1032 Corre, B., Lagabrielle, Y., Labaume, P., Fourcade, S., Clerc, C., Ballèvre, M., 2016.
1033 Deformation associated with mantle exhumation in a distal, hot passive margin
1034 environment: New constraints from the Saraillé Massif (Chaînons Béarnais, North-

Pyrenean Zone). Comptes Rendus Geosci. 348, 279–289. https://doi.org/10.1016/j.crte.2015.11.007

Crockford, P.W., Kunzmann, M., Bekker, A., Hayles, J., Bao, H., Halverson, G.P., Peng, Y., Bui, T.H., Cox, G.M., Gibson, T.M., Wörndle, S., Rainbird, R., Lepland, A., Swanson-Hysell, N.L., Master, S., Sreenivas, B., Kuznetsov, A., Krupenik, V., Wing, B.A., 2019. Claypool continued: Extending the isotopic record of sedimentary sulfate. Chem. Geol. 513, 200–225. https://doi.org/10.1016/j.chemgeo.2019.02.030

Curnelle, R., Dubois, P., 1986. Evolution mesozoique des grands bassins sedimentaires français; bassins de Paris, d'Aquitaine et du Sud-Est. Bull. la Société Géologique Fr. 8, 529–546.

Curnelle, R., Dubois, P., Seguin, J.C., Whitaker, D., Matthews, D.H., Roberts, D.G., Kent, P., Laughton, A.S., Kholief, M.M., 1982. The Mesozoic-Tertiary Evolution of the Aquitaine Basin [and Discussion]. Philos. Trans. R. Soc. London. Ser. A, Math. Phys. Sci. 305, 63–84.

Davies, G.R., Smith, L.B., 2006. Structurally controlled hydrothermal dolomite reservoir facies: An overview. Am. Assoc. Pet. Geol. Bull. 90, 1641–1690. https://doi.org/10.1306/05220605164

Dennis, K.J., Affek, H.P., Passey, B.H., Schrag, D.P., Eiler, J.M., 2011. Defining an absolute reference frame for "clumped" isotope studies of CO2. Geochim. Cosmochim. Acta 75, 7117–7131. https://doi.org/10.1016/j.gca.2011.09.025

Dickson, J.A.D., 1965. A Modified Staining Technique for Carbonates in Thin Section. Nature 205, 587–587. https://doi.org/10.1038/205587a0

Dunham, R.J., 1962. Classification of carbonate rocks according to their depositional texture, in: Ham, W.E. (Ed.), Classification of Carbonate Rocks. pp. 108–121.

Esquevin, J., Mendedez, R., Sourisse, C., 1987. Dosages Isotopiques S, C, O et H sur les

1060 fluides et les carottes d'une serie de puits de la ride Meillon - Pont d'As et de puits de
1061 Lacq Superieur. TOTAL EP internal report.

1062 Evans, M.A., Fischer, M.P., 2012. On the distribution of fluids in folds: A review of
1063 controlling factors and processes. J. Struct. Geol. 44, 2–24.
1064 https://doi.org/10.1016/j.jsg.2012.08.003

1065 Flügel, E., 2004. Microfacies of Carbonate Rocks. Springer Berlin Heidelberg, Berlin,
1066 Heidelberg. https://doi.org/10.1007/978-3-662-08726-8

1067 Folk, R.L., 1962. Spectral subdivision of limestone types. AAPG Spec. Publ. 1, 62–84.

1068 Fréchengues, M., Martini, R., Peybernès, B., Zaninetti, L., 1990. Mise en évidence
1069 d'associations de Foraminifères benthiques dans la séquence de dépôt ladino-
1070 ?carnienne du «Muschelkalk» des Pyrénées Catalanes (France, Espagne). Zaninetti,
1071 Louisette Publ. Comptes rendus l'Academie des Sci. II, Mécanique, Phys. Chim. Sci.
1072 l'univers, Sci. la terre. 310, 667–673.

1073 Gasparrini, M., Bakker, R.J., Bechstadt, T., 2006. Characterization of Dolomitizing Fluids
1074 in the Carboniferous of the Cantabrian Zone (NW Spain): A Fluid-Inclusion Study with
1075 Cryo-Raman Spectroscopy. J. Sediment. Res. 76, 1304–1322.
1076 https://doi.org/10.2110/jsr.2006.106

1077 Haile, B.G., Czarniecka, U., Xi, K., Smyrak-Sikora, A., Jahren, J., Braathen, A., Hellevang,
1078 H., 2018. Hydrothermally induced diagenesis: Evidence from shallow marine-deltaic
1079 sediments, Wilhelmøya, Svalbard. Geosci. Front.
1080 https://doi.org/10.1016/j.gsf.2018.02.015

1081 Haley, B.A., Klinkhammer, G.P., McManus, J., 2004. Rare earth elements in pore waters
1082 of marine sediments. Geochim. Cosmochim. Acta 68, 1265–1279.
1083 https://doi.org/10.1016/j.gca.2003.09.012

1084 Hinman, N.W., 1990. Chemical factors influencing the rates and sequences of silica phase

1085 transitions: Effects of organic constituents. Geochim. Cosmochim. Acta 54, 1563–
1086 1574. https://doi.org/10.1016/0016-7037(90)90391-W

1087 Houzay, J., Faggionato, J., Despujols, V., 2008. Maturity and source rock potential of the
1088 Albo-Aptian series. TOTAL EP internal report.

1089 Huntington, K.W., Eiler, J.M., Affek, H.P., Guo, W., Bonifacie, M., Yeung, L.Y.,
1090 Thiagarajan, N., Passey, B., Tripati, A., Daëron, M., Came, R., 2009. Methods and
1091 limitations of “clumped” CO2 isotope (Δ47) analysis by gas-source isotope ratio mass
1092 spectrometry. J. Mass Spectrom. 44, 1318–1329. https://doi.org/10.1002/jms.1614

1093 Huyghe, D., Mouthereau, F., Emmanuel, L., 2012. Oxygen isotopes of marine mollusc
1094 shells record Eocene elevation change in the Pyrenees. Earth Planet. Sci. Lett. 345–
1095 348, 131–141. https://doi.org/10.1016/j.epsl.2012.06.035

1096 Jammes, S., Lavier, L., Manatschal, G., 2010. Extreme crustal thinning in the Bay of
1097 Biscay and the Western Pyrenees: From observations to modeling. Geochemistry,
1098 Geophys. Geosystems 11. https://doi.org/10.1029/2010GC003218

1099 Jammes, S., Manatschal, G., Lavier, L., Masini, E., 2009. Tectonosedimentary evolution
1100 related to extreme crustal thinning ahead of a propagating ocean: Example of the
1101 western Pyrenees. Tectonics 28, n/a-n/a. https://doi.org/10.1029/2008TC002406

1102 Kitayama, Y., Thomassot, E., Galy, A., Golovin, A., Korsakov, A., D’Eyrames, E., Assayag,
1103 N., Bouden, N., Ionov, D., 2017. Co-magmatic sulfides and sulfates in the Udachnaya-
1104 East pipe (Siberia): A record of the redox state and isotopic composition of sulfur in
1105 kimberlites and their mantle sources. Chem. Geol. 455, 315–330.
1106 https://doi.org/10.1016/j.chemgeo.2016.10.037

1107 Koehrer, B.S., Heymann, C., Prousa, F., Aigner, T., 2010. Multiple-scale facies and
1108 reservoir quality variations within a dolomite body – Outcrop analog study from the
1109 Middle Triassic, SW German Basin. Mar. Pet. Geol. 27, 386–411.
1110 https://doi.org/10.1016/j.marpetgeo.2009.09.009

1111 Kroner, U., Romer, R.L., 2013. Two plates — Many subduction zones: The Variscan
1112 orogeny reconsidered. Gondwana Res. 24, 298–329.
1113 https://doi.org/10.1016/j.gr.2013.03.001

1114 Lagabrielle, Y., Labaume, P., de Saint Blanquat, M., 2010. Mantle exhumation, crustal
1115 denudation, and gravity tectonics during Cretaceous rifting in the Pyrenean realm (SW
1116 Europe): Insights from the geological setting of the lherzolite bodies. Tectonics 29.
1117 https://doi.org/10.1029/2009TC002588

1118 Lambert, L., Pernin, C., Maza, C., Virgone, A., 2006. Analyse sédimentologique,
1119 diagénétique et structurale du drain LA-415.G1. TOTAL EP internal report.

1120 Laurent, D., Gaucher, E., Christophe, D., Carpentier, C., Barré, G., Collon, P., Paris, G.,
1121 Pironon, J., 2019. A Sulfuric Acid Speleogenesis in the northern Pyrenees? Example
1122 of the Arbailles karstic region (West Pyrenees, France), in: Conference: EGU 2019.
1123 Vienna.

1124 Le Marrec, A., D'Aboville, O., Delahaye, S., Lagarigue, J., Moen Maurel, L., Dore, M.,
1125 Lang, J., 1995. Synthèse Géodynamique du Bassin d'Arzacq et de ses bordures.
1126 TOTAL EP internal report.

1127 Li, J., Duan, Z., 2011. A thermodynamic model for the prediction of phase equilibria and
1128 speciation in the H2O-CO2-NaCl-CaCO3-CaSO4 system from 0 to 250°C, 1 to 1000
1129 bar with NaCl concentrations up to halite saturation. Geochim. Cosmochim. Acta 75,
1130 4351–4376. https://doi.org/10.1016/j.gca.2011.05.019

1131 López-Horgue, M.A., Iriarte, E., Schröder, S., Fernández-Mendiola, P.A., Caline, B.,
1132 Corneyllie, H., Frémont, J., Sudrie, M., Zerti, S., 2010. Structurally controlled
1133 hydrothermal dolomites in Albian carbonates of the Ason valley, Basque Cantabrian
1134 Basin, Northern Spain. Mar. Pet. Geol. 27, 1069–1092.
1135 https://doi.org/10.1016/j.marpetgeo.2009.10.015

1136 Lucas, C., 1985. Le grès rouge du versant nord des Pyrénées: essai sur la géodynamique

de dépôts continentaux du Permien et du Trias. Univ. Toulouse.

Machel, H.., 2001. Bacterial and thermochemical sulfate reduction in diagenetic settings — old and new insights. Sediment. Geol. 140, 143–175. https://doi.org/10.1016/S0037-0738(00)00176-7

Machel, H.G., 2004. Concepts and models of dolomitization: a critical reappraisal. Geol. Soc. London, Spec. Publ. 235, 7–63. https://doi.org/10.1144/GSL.SP.2004.235.01.02

Machel, H.G., Anderson, J.H., 1989. Pervasive Subsurface Dolomitization of the Nisku Formation in Central Alberta. J. Sediment. Res. 59. https://doi.org/10.1306/212F90AC-2B24-11D7-8648000102C1865D

Mangenot, X., Bonifacie, M., Gasparrini, M., Götz, A., Chaduteau, C., Ader, M., Rouchon, V., 2017. Coupling Δ47 and fluid inclusion thermometry on carbonate cements to precisely reconstruct the temperature, salinity and δ18O of paleo-groundwater in sedimentary basins. Chem. Geol. 472, 44–57. https://doi.org/10.1016/j.chemgeo.2017.10.011

Mangenot, X., Gasparrini, M., Gerdes, A., Bonifacie, M., Rouchon, V., 2018a. An emerging thermochronometer for carbonate-bearing rocks: ∆47 /(U-Pb). Geology 46, 1067–1070. https://doi.org/10.1130/G45196.1

Mangenot, X., Gasparrini, M., Rouchon, V., Bonifacie, M., 2018b. Basin-scale thermal and fluid flow histories revealed by carbonate clumped isotopes (Δ 47) - Middle Jurassic carbonates of the Paris Basin depocentre. Sedimentology 65, 123–150. https://doi.org/10.1111/sed.12427

Masini, E., Manatschal, G., Tugend, J., Mohn, G., Flament, J.-M., 2014. The tectono-sedimentary evolution of a hyper-extended rift basin: the example of the Arzacq–Mauléon rift system (Western Pyrenees, SW France). Int. J. Earth Sci. 103, 1569–1596. https://doi.org/10.1007/s00531-014-1023-8

1162 Merino, E., Canals, A., 2011. Self-accelerating dolomite-for-calcite replacement: Self-
1163 organized dynamics of burial dolomitization and associated mineralization. Am. J. Sci.
1164 311, 573–607. https://doi.org/10.2475/07.2011.01

1165 Minami, H., Hachikubo, A., Yamashita, S., Sakagami, H., Kasashima, R., Konishi, M.,
1166 Shoji, H., Takahashi, N., Pogodaeva, T., Krylov, A., Khabuev, A., Kazakov, A., De
1167 Batist, M., Naudts, L., Chensky, A., Gubin, N., Khlystov, O., 2018. Hydrogen and
1168 oxygen isotopic anomalies in pore waters suggesting clay mineral dehydration at gas
1169 hydrate-bearing Kedr mud volcano, southern Lake Baikal, Russia. Geo-Marine Lett.
1170 38, 403–415. https://doi.org/10.1007/s00367-018-0542-x

1171 Moore, C.H., 2013. Carbonate Reservoirs, Second. ed. Elsevier, Amsterdam.

1172 Mountjoy, E.W., Green, D., Machel, H.G., Duggan, J., Williams-Jones, A.E., 1999.
1173 Devonian matrix dolomites and deep burial carbonate cements: A comparison
1174 between the Rimbey-Meadowbrook reef trend and the deep basin of west-central
1175 Alberta. Bull. Can. Pet. Geol. 47, 487–509.

1176 Passey, B.H., Levin, N.E., Cerling, T.E., Brown, F.H., Eiler, J.M., 2010. High-temperature
1177 environments of human evolution in East Africa based on bond ordering in paleosol
1178 carbonates. Proc. Natl. Acad. Sci. 107, 11245–11249.
1179 https://doi.org/10.1073/pnas.1001824107

1180 Passey, B.H., Levin, N.E., Cerling, T.E., Brown, F.H., Eiler, J.M., 2010. High-temperature
1181 environments of human evolution in East Africa based on bond ordering in paleosol
1182 carbonates. Proc. Natl. Acad. Sci. https://doi.org/10.1073/pnas.1001824107

1183 Pironon, J., Canals, M., Dubessy, J., Walgenwitz, F., Laplace-Builhe, C., 1998. Volumetric
1184 reconstruction of individual oil inclusions by confocal scanning laser microscopy. Eur.
1185 J. Mineral. 10, 1143–1150. https://doi.org/10.1127/ejm/10/6/1143

1186 Puigdefabregas, C., Souquet, P., 1986. Tectono-Sedimentary Cycles and Depositional
1187 Sequences of the Mesozoic and Tertiary from the Pyrenees. Tectonophysics 129,

173–203.

Renard, S., Pironon, J., Sterpenich, J., Carpentier, C., Lescanne, M., Gaucher, E.C., 2019. Diagenesis in Mesozoic carbonate rocks in the North Pyrénées (France) from mineralogy and fluid inclusion analysis: Example of Rousse reservoir and caprock. Chem. Geol. 508, 30–46. https://doi.org/10.1016/j.chemgeo.2018.06.017

Rosenbaum, J., Sheppard, S.M.., 1986. An isotopic study of siderites, dolomites and ankerites at high temperatures. Geochim. Cosmochim. Acta 50, 1147–1150. https://doi.org/10.1016/0016-7037(86)90396-0

Salardon, R., Carpentier, C., Bellahsen, N., Pironon, J., France-Lanord, C., 2017. Interactions between tectonics and fluid circulations in an inverted hyper-extended basin: Example of mesozoic carbonate rocks of the western North Pyrenean Zone (Chaînons Béarnais, France). Mar. Pet. Geol. 80, 563–586. https://doi.org/10.1016/j.marpetgeo.2016.11.018

Sansjofre, P., Cartigny, P., Trindade, R.I.F., Nogueira, A.C.R., Agrinier, P., Ader, M., 2016. Multiple sulfur isotope evidence for massive oceanic sulfate depletion in the aftermath of Snowball Earth. Nat. Commun. 7, 12192. https://doi.org/10.1038/ncomms12192

Schrijver, K., Williams-Jones, A.E., Bertrand, R., Chagnon, A., 1996. Genesis and controls of hydrothermal dolomitization in sandstones of the Appalachian thrust belt, Québec, Canada: Implications for associated galena-barite mineralization. Chem. Geol. 129, 257–279. https://doi.org/10.1016/0009-2541(95)00146-8

Serjouné, 1995. Bassin d'Arzacq, Aquitaine simulation de la maturite des roches mères. TOTAL EP internal report.

Sibley, D.F., Gregg, J.M., 1987. Classification of Dolomite Rock Textures. SEPM J. Sediment. Res. Vol. 57. https://doi.org/10.1306/212F8CBA-2B24-11D7-8648000102C1865D

1213 Sibson, R.H., Moore, J.M.M., Rankin, A.H., 1975. Seismic pumping—a hydrothermal fluid
1214 transport mechanism. J. Geol. Soc. London. 131, 653–659.
1215 https://doi.org/10.1144/gsjgs.131.6.0653

1216 Swart, P.K., Burns, S.J., Leder, J.J., 1991. Fractionation of the stable isotopes of oxygen
1217 and carbon in carbon dioxide during the reaction of calcite with phosphoric acid as a
1218 function of temperature and technique. Chem. Geol. Isot. Geosci. Sect. 86, 89–96.
1219 https://doi.org/10.1016/0168-9622(91)90055-2

1220 Swart, P.K., Cantrell, D.L., Westphal, H., Handford, C.R., Kendall, C.G., 2005. Origin of
1221 Dolomite in the Arab-D Reservoir from the Ghawar Field, Saudi Arabia: Evidence from
1222 Petrographic and Geochemical Constraints. J. Sediment. Res. 75, 476–491.
1223 https://doi.org/10.2110/jsr.2005.037

1224 Teixell, A., Labaume, P., Lagabrielle, Y., 2016. The crustal evolution of the west-central
1225 Pyrenees revisited: Inferences from a new kinematic scenario. Comptes Rendus
1226 Geosci. 348, 257–267. https://doi.org/10.1016/j.crte.2015.10.010

1227 Tremosa, J., Gailhanou, H., Chiaberge, C., Castilla, R., Gaucher, E.., Lassin, A., Gout, C.,
1228 Fialips, C., Claret, F., 2019. Effects of smectite dehydration and illitisation on
1229 overpressures in sedimentary basins: A coupled chemical and thermo-hydro-
1230 mechanical modelling approach. Mar. Pet. Geol. In press.
1231 https://doi.org/10.1016/j.marpetgeo.2019.08.021

1232 Tugend, J., Manatschal, G., Kusznir, N.J., 2015. Spatial and temporal evolution of
1233 hyperextended rift systems: Implication for the nature, kinematics, and timing of the
1234 Iberian-European plate boundary. Geology 43, 15–18.
1235 https://doi.org/10.1130/G36072.1

1236 Vacherat, A., Mouthereau, F., Pik, R., Bellahsen, N., Gautheron, C., Bernet, M., Daudet,
1237 M., Balansa, J., Tibari, B., Pinna Jamme, R., Radal, J., 2016. Rift-to-collision transition
1238 recorded by tectonothermal evolution of the northern Pyrenees. Tectonics 35, 907–

933. https://doi.org/10.1002/2015TC004016

Vandeginste, V., John, C.M., Manning, C., 2013. Interplay between depositional facies, diagenesis and early fractures in the Early Cretaceous Habshan Formation, Jebel Madar, Oman. Mar. Pet. Geol. 43, 489–503. https://doi.org/10.1016/j.marpetgeo.2012.11.006

Vilasi, N., Swennen, R., Roure, F., 2006. Diagenesis and fracturing of Paleocene–Eocene carbonate turbidite systems in the Ionian Basin: The example of the Kelçyra area (Albania). J. Geochemical Explor. 89, 409–413. https://doi.org/10.1016/j.gexplo.2005.11.018

Walls, R., Burrowes, G., 1985. The Role of Cementation in the Diagenetic History of Devonian Reefs, Western Canada. Thr Soc. Econ. Paleontol. Mineral.